South Australian Heat Flow Anomaly:
Source and implications for geothermal energy

Thesis submitted in accordance with the requirements of the University of Adelaide for an Honours Degree in Geophysics.

Michael Dello-Iacovo

November 2014

THE UNIVERSITY
*of*ADELAIDE

ABSTRACT

The South Australian Heat Flow Anomaly is a broad region (>400 km wide) in Protero-zoic South Australia defined by drill holes with anomalously high heat flow estimates yielding a mean of 92 +/- 10 mW m^{-2}, compared to a global Proterozoic mean of 49-54 mW m^{-2}. This study will conclusively determine the primary source of this anomalous heat flow. Thermal conductivities of 145 drill core samples have been measured using an optical thermal conductivity scanner. These were utilised with thermal conductivity and temperature profiles provided by Petratherm and the Department of State Development to make five new heat flow estimates in the Curnamona and Mount Painter provinces using the product and thermal resistance methods. Measured surface heat flows fall between 84.352 and 128.051 mW m^{-2}. Significant lateral variations in surface heat flow support previous work suggesting shallow crustal radiogenic heat generation, primar-ily in Mesoproterozoic high heat producing granites. Analysis of existing deep seismic data has revealed a significantly cooler and thicker lithosphere in the Proterozoic South Australia compared with regions dominated by mantle heat flow such as southeastern Australia. Geotherms have been computed for steady-state regimes to demonstrate that the surface heat flow evident in the South Australian Heat Flow Anomaly is consistent with elevated upper crustal source. Thick, thermally insulating sedimentary cover in the Curnamona and Mount Painter provinces and high temperatures at shallow depths are encouraging for geothermal energy exploration, and geothermal prospectivity for these provinces was examined. Lateral thermal conductivity variations of stratigraphies in the Curnamona Province have been assessed, revealing that more data must be collected to use thermal conductivity from neighbouring boreholes as a proxy for heat flow estimates.

Table of Contents

List of Figures

List of Tables

INTRODUCTION

Eastern Proterozoic South Australia possesses anomalously high surface heat flow. This region, including (from west to east) the eastern Gawler Craton, the Adelaide Rift Complex, the Curnamona Province (CP, revised from Curnamona Craton; Conor & Preiss, 2008), the Mount Painter Province (MPP), the western Delamerian Fold Belt and part of the Cooper Basin is termed the South Australian Heat Flow Anomaly (SAHFA). Though sparsely sampled (Matthews & Beardsmore, 2007), the SAHFA is defined by Neumann et al. (2000) as a broad region (>400 km wide) with heat flow of 92 $\pm$ 10 mWm^{-2}, significantly higher than the global Proterozoic mean of 49-54 mWm^{-2} (McLaren et al., 2003). While over 10,000 heat flow measurements have been made globally, 90% are from Europe, North America and southern Africa. South America, Asia and Australia have far fewer measurements, and Antarctica has virtually none (Neumann et al., 2000), resulting in a significant bias in the accepted mean global heat flow.

Neumann et al. (2000) and McLaren et al. (2003) propose that the SAHFA is primarily the result of elevated upper crustal heat generation in high heat producing (HHP) granites due to the high concentration of radiogenic elements and presence of a cold, thick lithosphere. However, the widespread nature of the SAHFA may suggest an elevated deep mantle heat input (M. Hand pers. comm. 2014), as broad half-widths of anomalies generally indicate deep sources.

This study aims to conclusively determine the source of this anomalous heat flow. We propose that voluminous suites of shallow crustal HHP granites are the primary source of the SAHFA. Consistently high mean basement heat generation (4.6 μWm^{-3}; Wyborn et al., 1998) supports this hypothesis. Lateral heat flow variations may provide information regarding a likely depth of thermal source, with changes over short distances

suggesting shallow sources and changes over long distances suggesting deeper sources (Reiter, 2008).

Temperature profiles and thermal conductivity measurements of drill core are taken from four drill holes in the CP, and temperature and thermal conductivity data for Paralana 1B in the MPP are provided by Petratherm. Temperature profiles for CP holes are logged by the Department of Water, Land and Biodiversity Conservation (DWLBC), and an optical thermal conductivity scanner (TCS) is used to measure thermal conductivity. An analysis of this relatively new method is undertaken to ensure its validity. Thermal conductivity measurements of CP stratigraphic packages from different holes are compared to examine whether thermal conductivity measurements of stratigraphies can be used as a proxy between holes. The effects of sample saturation on thermal conductivity measurements are assessed to determine the effect on measurement of achieving *in situ* conditions. Porosities of samples are measured to estimate how thermal conductivity measurements are likely to be affected by saturation.

Surface heat flow is estimated from temperature gradient and thermal conductivity using both the product (e.g. Lam et al., 1982) and thermal resistance (Bullard, 1939) methods to expand the SAHFA heat flow database. Heat flow measurements are compared to local sites and put into a regional context. Existing heat generation and seismic data are examined and previous studies are reviewed to suggest a source of elevated heat flow. A family of steady-state geotherms are modelled using the Hasterok & Chapman (2011) method to demonstrate that the lithospheric thickness observed in Proterozoic southern Australia is consistent with elevated crustal heat generation. The lateral variation of heat flow in the SAHFA is compared to other global regions where the thermal source is better defined.

The SAHFA is a highly prospective target for geothermal energy exploration due to high temperatures at shallow depths and thick, insulating sedimentary cover (Matthews,

2009). The geothermal potential of the SAHFA, with particular emphasis on the CP and MPP, is discussed using data acquired in this study.

GEOLOGICAL SETTING

The new data were collected in the Proterozoic CP and neighbouring MPP (Figure 1). These provinces were separated from the initially contiguous Gawler Craton (Wade et al., 2012) by the ca. 820 Ma failed Adelaide Rift Complex (Wingate et al., 1998), consisting of Palaeo- to Mesoproterozoic basement granites and gneisses, and overlain by Neoproterozoic to Cambrian sedimentary cover (Coats & Blissett, 1971; Preiss, 1990). The Gawler Craton is a stable Archaean to Mesoproterozoic terrane (Neumann et al., 2000). It hosts zones of radiogenically enriched iron oxide deposits, particularly in the Olympic Province.

The CP consists of Palaeoproterozoic to Mesoproterozoic sediments, granites and volcanics, notably the Benagerie Ridge Volcanic Suite (BVS; Wade et al., 2012). The CP is relatively stable and unaffected by recent tectonic processes (e.g. Sandiford, 2003).

The MPP, north of the CP, is divided into the Mount Painter and Mount Babbage inliers (Kromkhun et al., 2013). The basement is the ca. 1595 ± 3.7 Ma (Armit et al., 2014) Radium Creek Group (revised from Radium Creek Metamorphics; Preiss et al., 2010) comprised of interbedded felsic volcanics (Kromkhun et al., 2013). The basements of the CP and MPP are interpreted as a distinct blocks (Armit et al., 2014), separated by a major southeast-dipping discontinuity (Korsch, 2010) which includes the Paralana Fault. Felsic tuffs belonging to the BVS are intersected at $\sim$3950 m depth in geothermal well Paralana 2 in the Mount Painter Inlier (Reid et al., 2011), suggesting common stratigraphy at depth.

The Proterozoic basement of the SAHFA is highly enriched in radiogenic elements, primarily hosted in HHP granites. The basement is unconformably overlain by thick

3

Neoproterozoic and younger sedimentary cover of clastics, carbonates and volcanics. Cover is especially thick in the Adelaide Rift Complex, resulting in an absence of heat generation data for this province (Neumann et al., 2000).

NEW SITE DESCRIPTIONS

Frome 8

This shallow borehole (500 m) traverses dolomitic siltstones with minor interbedded shales to around 400 m depth and fine-grained sandstone interbedded with fine conglomerates and greywacke to the end of hole. Temperature was sampled every 0.05 m to a depth of 500 m 47 days after completion of hole.

Frome 9

This shallow borehole (505 m) traverses clays to 92 m, fine grained dolomitic limestones to 112 m and, shales, dolomitic siltstones and dolomites to the end of hole. Temperature was sampled every 0.05 m to a depth of 500 m 51 days after completion of hole.

Frome 12

This deep borehole (1761 m) traverses a stratigraphy of siltstones, dolomites, sandstones and limestones to 1471 m then fractured granite with some gneissic material until the end of hole. Temperature was sampled every 0.05 m. Initial temperature logging took place 3 days after the temporary cessation of drilling, with the remainder of the hole logged 3 days after the total depth was reached. Temperature logs exist to a depth of 1010 m.
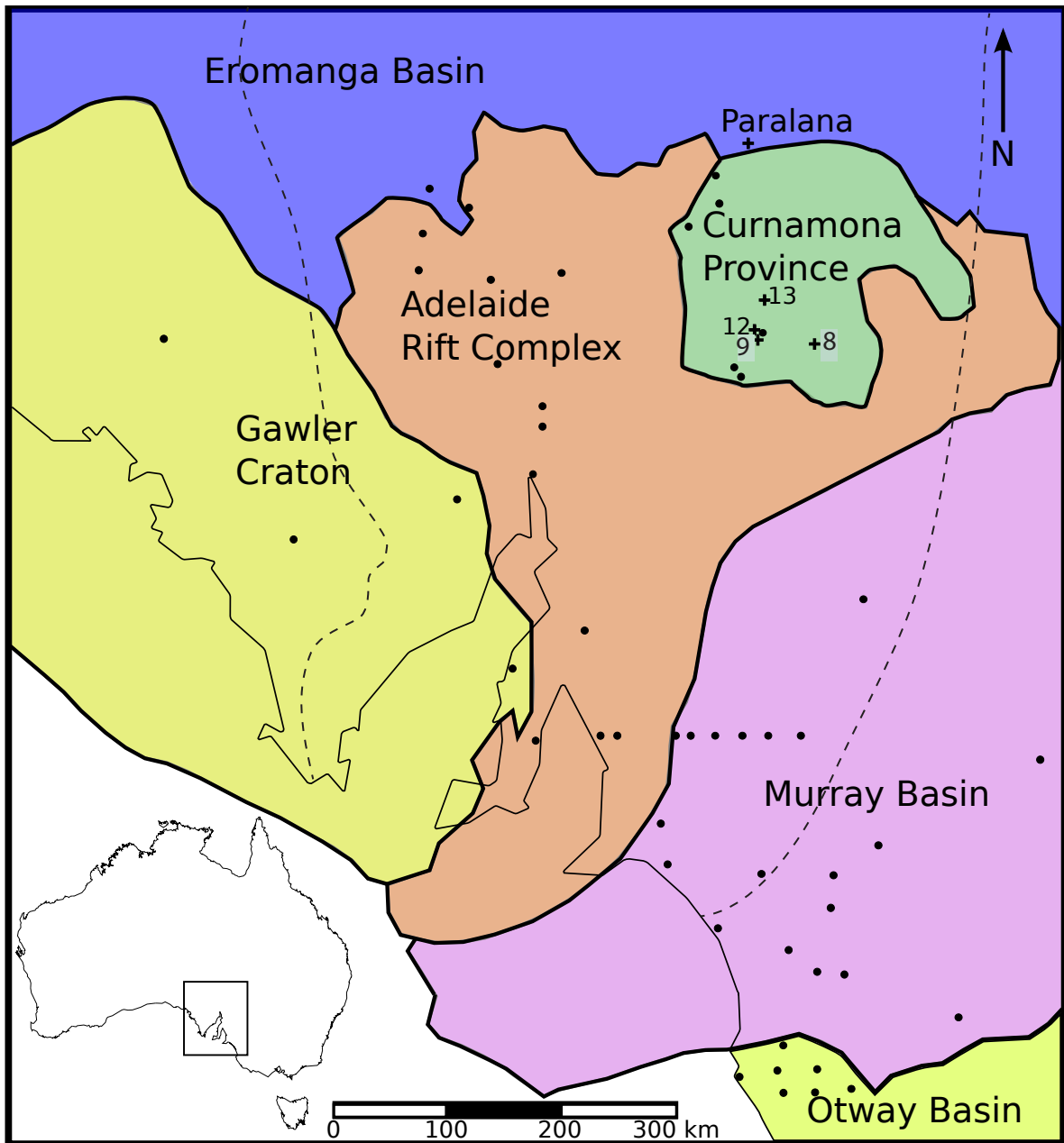
Figure 1: Major geological provinces of southern Australia with locations of previous heat flow measurements (D. Hasterok pers. comm. 2014) displayed as points. Locations of heat flow measurements made in this study, Frome 8, 9, 12, 13 and Paralana 1B are displayed as crosses. The outline of the SAHFA is depicted by the dashed line. Geological provinces and drill hole locations are plotted using GMT (Wessel et al., 2013).

Frome 13

This deep borehole (1809 m) traverses a typical sedimentary sequence to 1703 m then the BVS until the end of hole. Temperature was sampled irregularly from depths of 465 m to 1809 m, averaging 80 m between each measurement. Temperature was logged 4 days after the completion of hole.

Paralana 1B

This deep borehole (1807.5 m) is drilled in the MPP and traverses a series of sedimentary rocks including shales, mudstones, sandstones and limestones. Temperature was sampled from 280 m to 1820 m every 1 m. Temperature was logged $\sim$75 days after the completion of hole.

METHODS

The drill holes utilised in this project were selected for their locality within the SAHFA and the availability of drill core and temperature profiles, provided by the Department of State Development (DSD) and Petratherm Ltd. All uncertainties were propagated using the general formula of Bevington (1969):

$$\sigma = \left(\sum_{i=1}^{N} \sigma_i^2 \left(\frac{\partial f}{\partial x_i} \right)^2 \right)^{\frac{1}{2}}, \tag{1}$$

The derivation of error propagation for individual equations is detailed in Appendix D.

Temperature

Temperature profiles of Frome drill holes were logged by the Department of Water Lands and Biodiversity Conservation (DWLBC) using a T12 probe. Temperature was sampled

every 0.05 m with a relative uncertainty at 23 °C of ± 0.87%. Temperature profiles of Paralana drill holes were logged by Baker Hughes using a Kuster probe with accuracy of ± 0.354 °C and resolution of 0.001 °C. Temperature was filtered using an averaging window. The size of the averaging window was determined on a case-by-case basis for each hole. It was increased until the noise resultant from precision limitations was removed and the profile remaining was deemed to represent the true temperature profile. Thermal gradient (mK m^{-1}) is defined by:

$$\Gamma = \frac{\Delta T}{\Delta z},\tag{2}$$

where ΔT is the change in temperature and Δz is the change in depth.

A thermal gradient profile was plotted for each hole using the filtered temperature data. The mean thermal gradient for a stratigraphic package was determined by taking the gradient of the temperature from the top of the package to the bottom. Thermal gradients within and below the zone of surface climatic influence are determined separately. Reduced temperature is plotted and used to determine the depth at which surface climatic effects decay to negligible levels. Using filtered temperature data, reduced temperature at depth z (m) was plotted with the equation:

$$T_r = \frac{\Gamma_t z}{1000} - T_s,\tag{3}$$

where Γ_t is the mean temperature gradient over the total depth of hole not affected by surface climatic effects and T_s (°C) is the surface temperature.

Porosity

Density and interconnected porosity of the core samples were estimated to examine the relationship between interconnected porosity and thermal conductivity. Samples were

weighed dry and suspended in water by a string. Weights were measured using a triple beam balance with a stated precision of $\pm$ 0.1 g. The core was then saturated with water in a vacuum at a pressure of $\sim$-100 kPa for over 4 hours and weighed again. The following equations were used to determine density and interconnected porosity for each sample:

$$\frac{\rho_{rock}}{\rho_{water}} = \frac{M_{coredry}}{M_{coredry} - M_{corewet}}, \tag{4}$$

$$\rho_{unsat} = \rho_{matrix}(1 - \phi) + \phi\rho_{air}, \tag{5}$$

where ϕ is interconnected porosity, ρ is density and M is mass. This method is detailed in Balco & Stone (2003).

Thermal conductivity

Thermal conductivity may be measured using the steady-state divided bar method (e.g. Blackwell & Spafford, 1987), the half-space line-source method (Carslaw & Jaeger, 1947), and more recently the transient heat-source optical scanning method (e.g. Popov, Pribnow, Sass, Williams & Burkhardt, 1999). The deviation of results from these methods is generally <4%, primarily due to sample inhomogeneity (Popov, Pribnow, Sass, Williams & Burkhardt, 1999). The optical Thermal Conductivity Scanner (TCS), developed by Lippmann Geophysical Instruments based on the method of Popov et al. (1985), was used to measure thermal conductivity of samples in this study. The TCS can measure thermal conductivities from 0.2 to 25 $Wm^{-1}K^{-1}$ with machine precision of $\pm$ 3% and spatial resolution of 2-3 mm. Measurement uncertainties were generated by the TCS software for individual samples. The use of measurement standards (Table 1) negated the machine uncertainty, and so uncertainties of samples were interpreted to be the measurement uncertainties.

Table 1: Properties of the reference standards utilised in determining thermal conductivity.

Standard	Material	λ at 20 °C $(\mathbf{Wm^{-1}K^{-1}})$	κ $(\mathbf{m^2s^{-1}})$
1	Glass	0.709	0.401
2	Fused Quartz	1.350	0.850
3	Gabbro	2.370	1.020
4	Titanium Alloy	5.940	2.685
5	Steel	13.30	3.619
Corning 7980	Fused Silica	1.389	0.750

λ is the standard's thermal conductivity and κ is the thermal diffusivity.

Measured conductivity is representative of a sample to a depth below its surface that increases with conductivity (Popov, Kiselev & Mordvinova, 1999), thus the true mean conductivity of each sample was not achieved. The optical scanning method was used in this study for its advantages, including high sampling rate and contactless, non-destructive measurements. To ensure that varying reflective properties of minerals did not impact thermal conductivity measurements, a 20-30 mm wide, 25-40 μm thick black stripe was painted down the length of each sample using White Knight branded water-based matte acrylic paint. Samples measured on their curved surface were placed on metal props to ensure they did not dip below the scanning stage, leading to a systematic bias due to a reduced distance to the heat source.

Thermal conductivity of Frome samples were measured dry and saturated. Where thermal conductivity was measured on a curved surface, measured conductivity was multiplied by a correction factor to remove the associated systematic bias, interpreted to result from differences in heat diffusion and cooling dynamics between planar and cylindrical surfaces (Bowker, 2013). The correction factors are 1.057 for HQ sized cores with measured conductivity <4 $Wm^{-1}K^{-1}$, 1.071 for HQ sized cores with measured conductivity >4 $Wm^{-1}K^{-1}$, 1.051 for NQ sized cores with measured conductivity <3.5

$Wm^{-1}K^{-1}$, and 1.056 for NQ sized cores with measured conductivity >3.5 $Wm^{-1}K^{-1}$. The derivation of these correction factors are detailed in (Bowker, 2013).

Thermal conductivities measurements and uncertainties of Paralana samples were provided by Hot Dry Rocks Pty Ltd using a divided bar. Samples were split into three sub-samples which were individually measured to reduce uncertainty and minimise the effects of inhomogeneity. An error floor of $\pm$ 3 % for Frome samples and $\pm$ 5 % for Paralana samples was set to account for the uncertainty inherent in determining the conductivity of a stratigraphic package.

Temperature and pressure are known to affect thermal conductivity (Lee & Deming, 1998), though how they are affected remains contentious (Midttømme & Roaldset, 1999). Both increases (Anand et al., 1973; Gilliam & Morgan, 1987) and decreases (Balling et al., 1981; Demongodin et al., 1991) in thermal conductivity have been observed with rising temperature. Conductivity of water generally increases with temperature while conductivity of most minerals decreases with temperature (Midttømme & Roaldset, 1999).

Corrections were made to lab measurements of thermal conductivity in this study for samples from depths where temperature data exist to account for *in situ* temperature. Two correction methods are shown in Figure 2. The choice of correction method may have a significant impact on thermal conductivity, and therefore heat flow estimates. The Chapman et al. (1984) method was used to correct thermal conductivity for temperature in this study:

$$\lambda_T = \lambda_{20} \left(\frac{293}{T + 273} \right),\tag{6}$$

where λ_{20} is the thermal conductivity measured at room temperature (assumed to be 20 °C) and T is *in situ* temperature of the sample. A second equation is used by Chapman et al. (1984) to correct for the thermal conductivity of water in the pore space. This equation was not used in this study, as it was determined that the porosities of
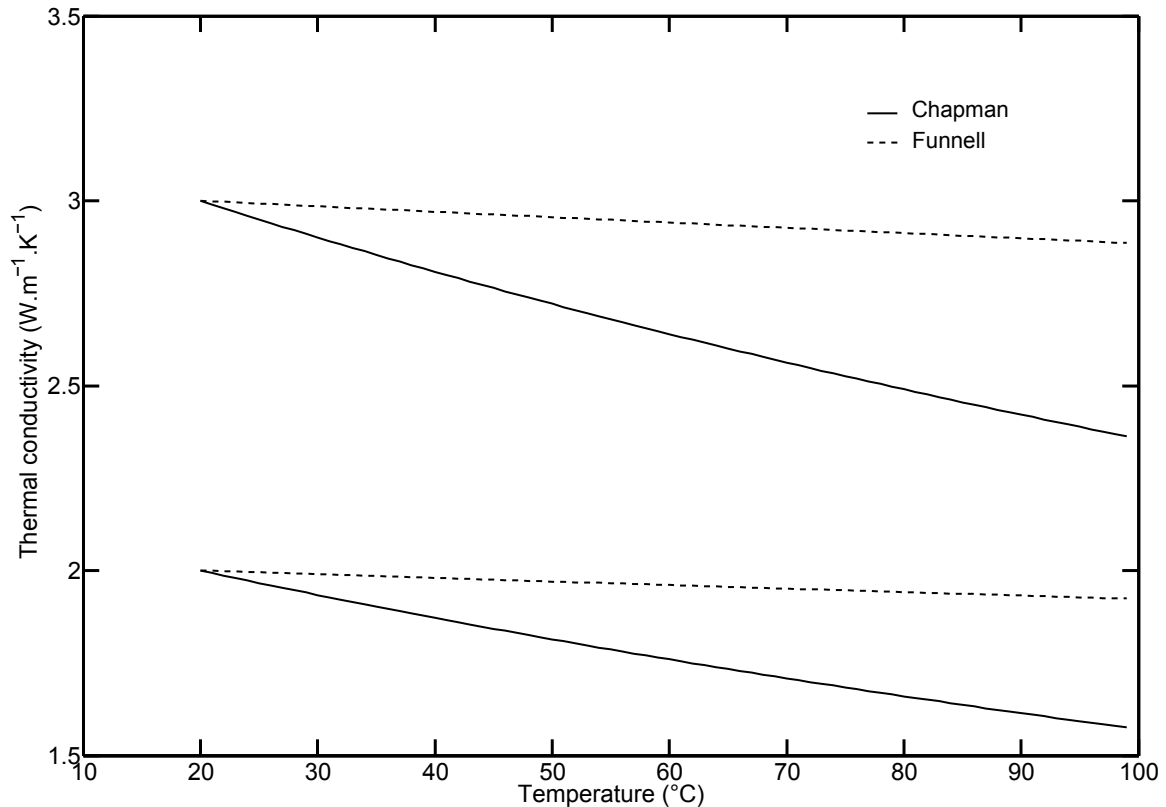
Figure 2: The Chapman et al. (1984) and Funnell et al. (1996) models for temperature correction of thermal conductivity are displayed for two theoretical samples of 2 and 3 $Wm^{-1}K^{-1}$. Both models assume a lab measurement of conductivity at 20 °C.

samples were low enough for this effect to be ignored. Chapman et al. (1984) states that for sample conductivities from 1.5 to 3.5 $Wm^{-1}K^{-1}$, 10 % porosity adjusts measured conductivity by 9 to 16 %. Measured porosities of Frome drill holes show a mean of 0.6 % and a maximum of 4.1 %. 79 % of measured samples show less than 1 % porosity. No porosity data were made available for Paralana 1B samples, and so the effect of porosity could not be considered. The Chapman et al. (1984) model was selected as it does not require individual correction factors for varying rock types. It is therefore more generalised than other models, however is easier to apply to large numbers of samples. A number of studies have successfully employed the Chapman et al. (1984) method (e.g. Deming & Chapman, 1988a; Deming & Chapman, 1988b).

11

Thermal conductivities of stratigraphies were determined using the harmonic mean of each thermal conductivity measurement within the package, weighted by the distance of a measurement to the nearest measurement above and below. Samples are assumed to be representative of a package for half the distance between itself and the next samples above and below. When a sample is the upper or lowermost for a given package, it is assumed to be representative to the top or bottom of the package respectively. By the harmonic mean equation, the average conductivity of a stratigraphy is:

$$\lambda_{av} = \sum_{i=1}^{N} \frac{h_t}{\left(\frac{h_i}{\lambda_i}\right)}, \tag{7}$$

where h_t is the total thickness of the package, h_i is the distance over which a sample of conductivity λ_i is assumed to be representative.

The harmonic mean is valid for holes in this project as they are vertically drilled through a sequence of sub-horizontal strata, with each bed having a different thermal conductivity. This allows the assumption to be made that the stratigraphies are layered perpendicularly to the direction of heat flow, and that heat flow is one-dimensional and vertical (Cull & Beardsmore, 2001).

Heat flow

Heat flow was determined for each stratigraphic package intersected using the product method:

$$Q_i = \lambda_i \Gamma_i, \tag{8}$$

where Q is the heat flow, λ is the mean thermal conductivity for an interval and Γ_t is the thermal gradient for an interval.

Heat flow was also determined using the thermal resistance method, an estimate of heat flow based on thermal resistance, R, defined as:

$$R = \sum_{i=1}^{N} \frac{h_i}{\lambda_i}, \tag{9}$$

with units of $\text{m}^2 \text{ KW}^{-1}$ and where h_i is the thickness of an interval. Thermal resistance is a measure of how effectively a volume of material retards the flow of heat (Gallagher, 1990). Thermal resistance is plotted against temperature for each hole, with the slope between two points indicating the heat flow in that interval. By the method of Chapman et al. (1984), linear regression is plotted for all points for each hole to estimate the surface heat flow. Results from both methods are compared to ensure the validity of each heat flow measurement. The zero point of thermal resistance is arbitrarily set at the top of the shallowest stratigraphic package, so that the cumulative thermal resistance is representative of the stratigraphic package from this point to a given depth. Sparse temperature and thermal conductivity data spacing in Frome 13 required that heat flow be determined for intervals where sufficient data exist. Surface heat flow for a hole is taken as the arithmetic mean of each interval measured. Intervals that appear to show spurious errors are not included in this calculation. Further details on how these methods were carried out can be found in Appendix B.

OBSERVATIONS AND RESULTS

The drill holes in this project are summarised in Table 2, including thermal gradient and thermal conductivity estimates for each stratigraphy where data were acquired.

Table 2: Summary of drill holes utilised in this project.

Hole name	Hole ID	Latitude (°N)	Longitude (°E)	Elevation (m)	Total depth (m)	Interval (m)	Formation	Mean thermal gradient (mK m^{-1})	N_λ	Mean thermal conductivity (Wm^{-1}K^{-1})
Frome 8	218427	-31.712	140.330	134	500	200-477	Amberoona	27.195 ± 1.441	28	3.102 ± 0.025
Frome 9	230974	-31.690	139.823	111	505	92-310	Amberoona	40.817 ± 1.832	21	2.916 ± 0.030
Frome 12	239792	-31.598	139.79	92	1761	310-493	Etina	32.333 ± 2.667	22	2.787 ± 0.041
						134.3-949.8	Brachina	43.041 ± 0.775	14	2.975 ± 0.033
						949.8-965.8	Nuccaleena	37.500 ± 50.830	2	3.371 ± 0.080
						965.8-1145	Elatina		4	3.668 ± 0.073
						1172.8-1419	Etina		5	3.278 ± 0.049
						1419-1471.1	Upalinna		3	3.160 ± 0.086
						1471.1-1761.2	Granite		4	3.165 ± 0.082
Frome 13	241847	-31.375	139.881	61	1809	206-384.5	Wirrealpa		2	2.750 ± 0.060
						384.5-857.3	Billy Creek		5	3.140 ± 0.065
						857.3-978.6	Wilkawillina		4	2.800 ± 0.063
						978.6-1426.8	Brachina		5	3.080 ± 0.209
						1434.5-1537.3	Elatina		2	3.580 ± 0.085
						1537.3-1703	Etina		6	3.192 ± 0.083
						1703-1809.3	BVS		2	3.523 ± 0.088
Paralana 1B	211843	-30.210	139.713	44	1807.5	518.3-698	Sandstone	23.407 ± 2.786	6	4.446 ± 0.450
						775.6-835.6	Mudstone	40.497 ± 8.341	2	2.809 ± 0.106
						993-1039.8	Arkosic sst.	26.603 ± 10.695	3	4.214 ± 0.169
						1081.1-1196.5	Shale	52.193 ± 4.336	5	1.848 ± 0.046
						1242.8-1327.5	Calc. mudst.	32.853 ± 5.907	4	3.668 ± 0.094
						1357.2-1525.5	Mudstone	44.241 ± 2.974	5	2.424 ± 0.172
						1620.2-1752.1	Shale	49.057 ± 3.796	3	2.075 ± 0.063

Mean thermal gradient is determined using the temperature measurements at the top and bottom of each stratigraphic package. Temperature data did not exist for Frome 12 at a depth greater than 1002 m and temperature was insufficiently sampled to provide an estimate of thermal gradient for Frome 13. Mean thermal conductivity of each package is determined by the harmonic mean of each measurement. N_λ refers to the number of samples used to determine thermal conductivity for each interval.

Temperature

Raw and filtered temperature data for Frome 8, 9, 12, 13 and Paralana 1B and 2 are presented in Figures 3 through 7. Temperature data are filtered using a windowing method. Filtered temperature data were used to plot the thermal gradient and reduced temperature. Thermal gradient and reduced temperature are not plotted for Frome 13 due to insufficiently sampled temperature, while reduced temperature is not plotted for Paralana 1B as temperature data were not sampled above 277 m, and therefore surface climatic effects are assumed not to affect the measurements.

Small intervals generally yield high errors in temperature gradient and therefore heat flow. The Nuccaleena Dolomite intersected in Frome 12 is 16 m thick. The difference in temperature between the top and bottom measurements for this formation is small, which combined with the small interval length yields a high error of 50.830 mK m^{-1} in comparison to the thermal gradient of 37.500 mK m^{-1}. This demonstrates a significant limitation, and thus the Nuccaleena Dolomite was not used to determine heat flow. Longer intervals for temperature gradient determination are ideal for reducing error.

Thermal conductivity

Dry and saturated thermal conductivities for Frome samples were measured using the TCS, while the Paralana 1B core samples were measured by Hot Dry Rock Pty Ltd with a divided bar. Conductivities of individual samples and stratigraphies are displayed in Figures 3 through 7. Thermal conductivities pre- and post-temperature correction are displayed where temperature data were available to correct for *in situ* temperature. Raw thermal conductivity data are displayed in Appendix C.

The accuracy of thermal conductivity estimates for a stratigraphic package is limited by the sampling rate. A thermal conductivity mean was calculated for each stratigraphy, however it is apparent that the conductivity varies throughout. To an extent this

can be partially resolved by increasing the number of samples measured, however as evidenced in the Etina Formation intersected in Frome 9 (Figure 4), significant spread occurs which cannot be accounted for by simply increasing sample population. For example, the Amberoona Formation intersected in Frome 8 (Figure 3), while logged as a single formation, measurements appear to reveal three discrete intervals over which the conductivities show a higher degrees of consistency.

COMPARISON OF DRY AND SATURATED DRILL CORE THERMAL CONDUCTIVITIES

Thermal conductivity saturation models are discussed in (Somerton, 1992), where conductivity is shown to decrease with increasing porosity for both saturated and unsaturated samples. Conductivities are expected to be higher for saturated samples (Popov, Kiselev & Mordvinova, 1999), as water ($\sim$0.6 Wm^{-1}K^{-1}; Ramires et al., 1995) has higher conductivity than air ($\sim$0.025 Wm^{-1}K^{-1}; Balandin, 2008). This effect is expected to be greater for samples with higher porosity, as a greater volume of air is replaced.

Dry and saturated measurements of thermal conductivity for Frome 8, 9, 12 and 13 are compared in Figure 8 to demonstrate the effect of saturating samples to achieve *in situ* conditions. A high degree of scatter is observed in dry and saturated conductivities for all Frome drill holes. Dry conductivity measurements tend to plot higher than the corresponding saturated measurement for Frome 8, 9 and 12, which is unusual and in contrast to the relationship expected. The low porosities in the samples for these holes may provide some explanation. Given a sufficiently low porosity, the scatter from uncertainty in thermal conductivity measurements will partially overcome any trend from the saturation of core. The scatter observed, however, is greater than the uncertainty in conductivity measurements, indicating that another explanation is necessary.

As Frome 12 and 13 were measured several months before Frome 8 and 9, the possibility of an altered method must be considered, however this is unlikely as each hole

Figure 3: Frome 8 temperature (a), thermal gradient (b), reduced temperature (c), saturated thermal conductivity (d) and heat flow (e) plotted vs depth. Temperature data were acquired using the T12 probe by the Department of Water, Land and Biodiversity Conservation at 50 mm intervals. Uncertainties in temperature and thermal gradient are less than the thickness of the line and so are not displayed. The thermal gradient was determined for a given depth by using a window with size of 500 data points. The rapid variation in thermal gradient at the top of the hole is due to surface climatic and circulation effects. The reduced temperature is plotted and demonstrates that surface effects decay at ~61 m. The linear temperature-depth variation equation used to plot the reduced temperature is: $T(z) = 27.00\ z/1000 - 22.90$. Conductivities and uncertainties of 28 samples have been measured using the TCS. Individual conductivity measurements before and after temperature correction are displayed. A weighted harmonic mean has been used to determine the thermal conductivity. The grey box indicates the standard deviation of the stratigraphy's thermal conductivity. Mean heat flow for the Amberoona Formation is determined using the product method, taking the harmonic mean of thermal conductivity for the package and using the temperature at the top and bottom of the package to acquire the thermal gradient. Dashed lines indicate potential changes in stratigraphy, possibly boundaries of sub-groups.

17

Figure 4: Frome 9 temperature (a), thermal gradient (b), reduced temperature (c), saturated thermal conductivity (d) and heat flow (e) plotted vs depth. Temperature data were acquired using the T12 probe by the Department of Water, Land and Biodiversity Conservation at 50 mm intervals. Uncertainties in temperature and thermal gradient are less than the thickness of the line and so are not displayed. The thermal gradient was determined for a given depth by using a window with size of 500 data points. The rapid variation in thermal gradient at the top of the hole is due to surface climatic and circulation effects. The reduced temperature is plotted and demonstrates that surface effects decay at ~84 m. The linear temperature-depth variation equation used to plot the reduced temperature is: T(z) = 38.00 z/1000 - 24.20. Conductivities and uncertainties of 48 samples have been measured using the TCS. Individual conductivity measurements before and after temperature correction are displayed. A weighted harmonic mean has been used to determine the thermal conductivity of stratigraphies. The grey box indicates the standard deviation of the stratigraphy's thermal conductivity. Thermal conductivity measurements are corrected for *in situ* temperature. Mean heat flow has been determined for each stratigraphy using the product method, taking the harmonic mean of thermal conductivity for the package and using the temperature at the top and bottom of the package to acquire the thermal gradient.
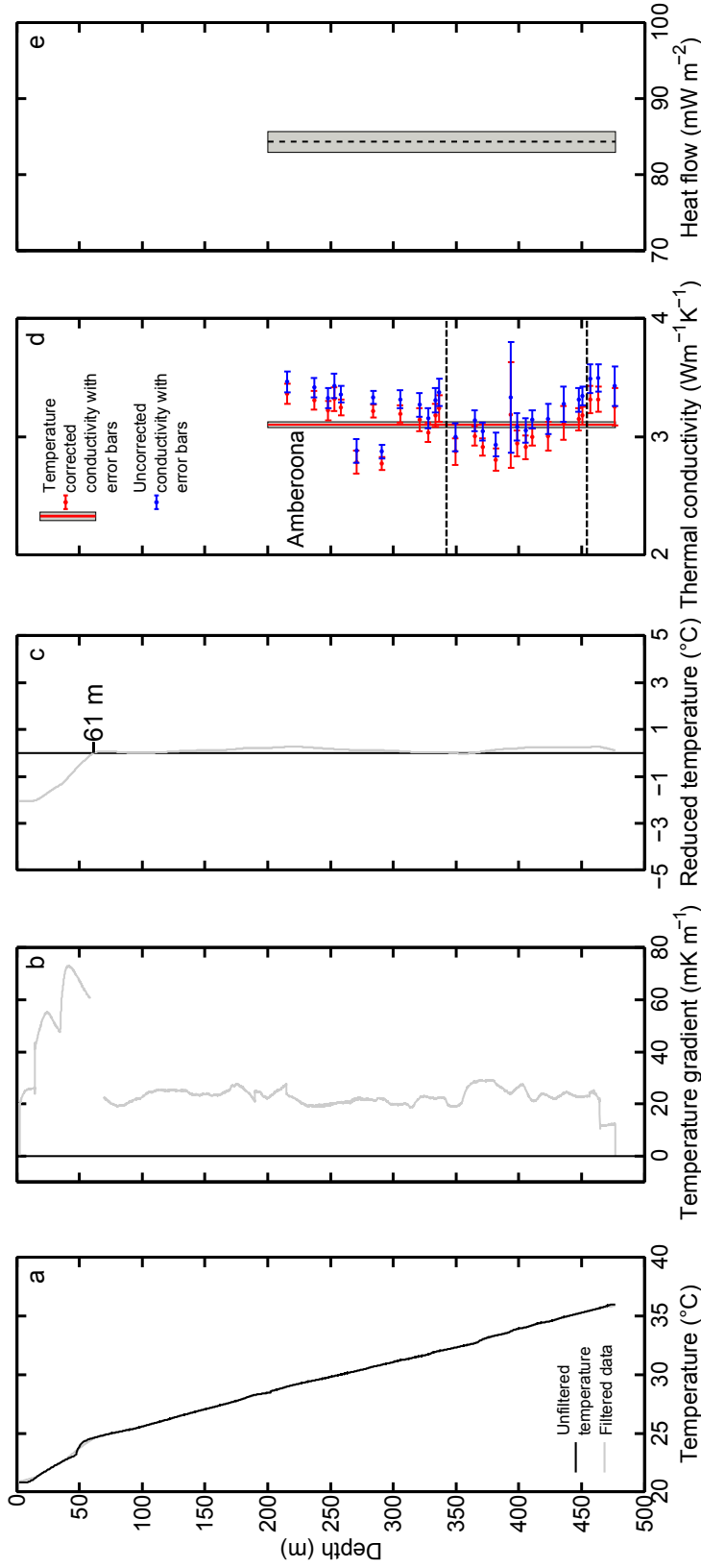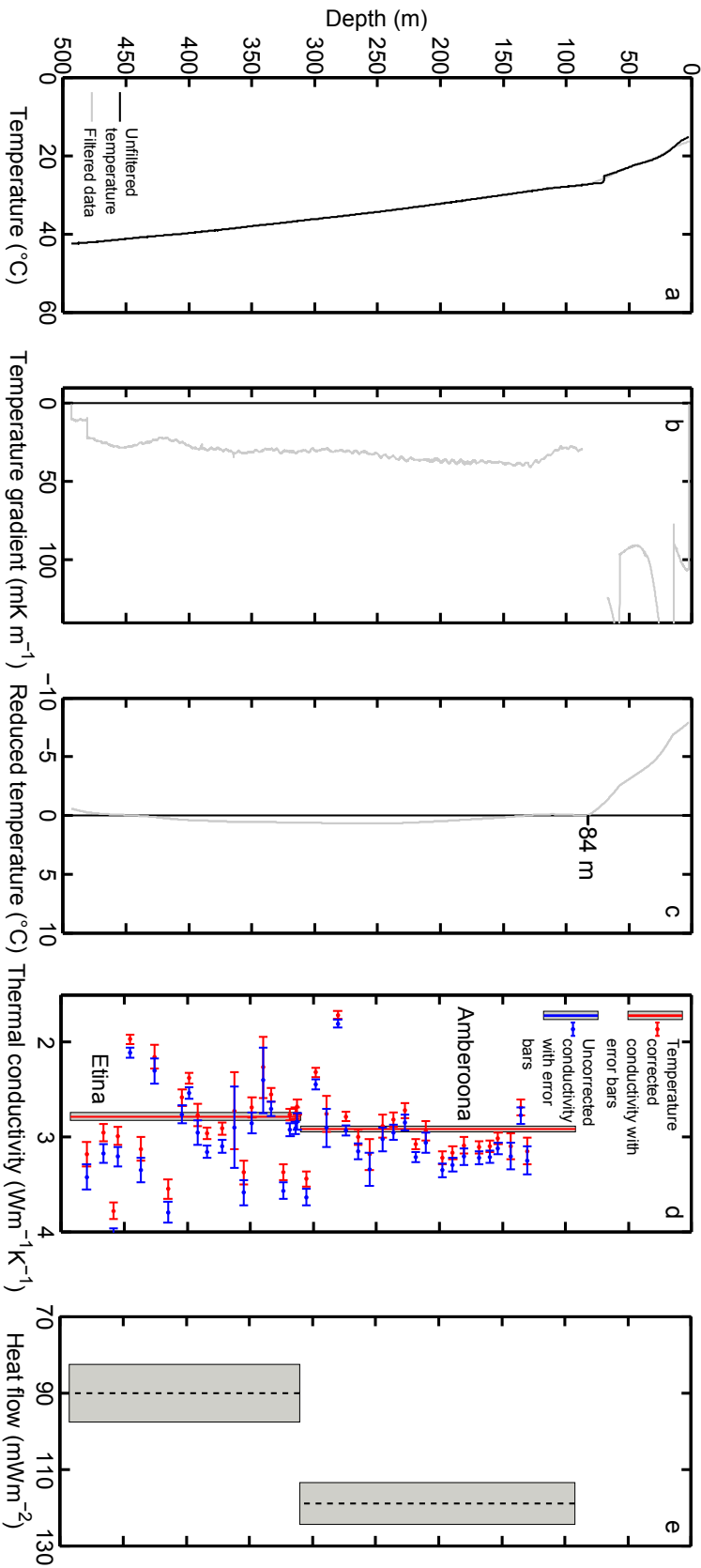
Figure 5: Frome 12 temperature (a), thermal gradient (b), reduced temperature (c), saturated thermal conductivity (d) and heat flow (e) plotted vs depth. Temperature data were acquired using the T12 probe by the Department of Water, Land and Biodiversity Conservation at 50 mm intervals. Uncertainties in temperature and thermal gradient are less than the thickness of the line and so are not displayed. The thermal gradient was determined for a given depth by using a window with size of 500 data points. The rapid variation in thermal gradient at the top of the hole is due to surface climatic and circulation effects. The reduced temperature is plotted and demonstrates that surface effects decay at ∼113 m. The linear temperature-depth variation equation used to plot the reduced temperature is: $T(z) = 43.00 \ z/1000 - 25.00$. Conductivities and uncertainties of 32 samples have been measured using the TCS. Individual conductivity measurements before and after temperature correction are displayed. A weighted harmonic mean has been used to determine the thermal conductivity of the formations traversed. The grey box indicates the standard deviation of the stratigraphy's thermal conductivity. Temperature data were only available to 1000 m and so only the Brachina Formation and Nuccaleena Dolomite have been corrected for in situ temperature. Mean heat flow has been determined for each stratigraphy using the product method, taking the harmonic mean of thermal conductivity for the package and using the temperature at the top and bottom of the package to acquire the thermal gradient.
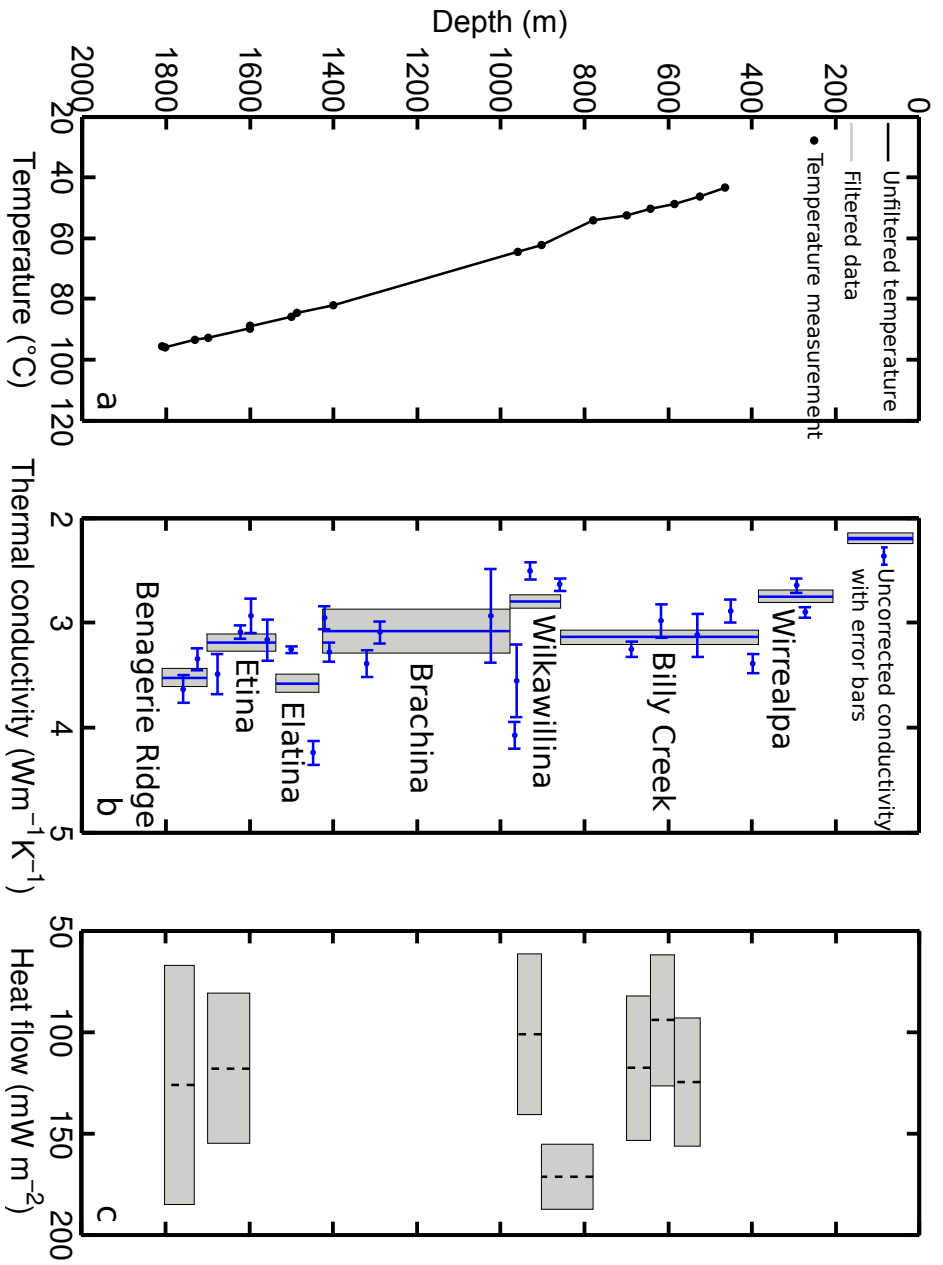
Figure 6: Frome 13 temperature (a), saturated thermal conductivity (b) and heat flow (c) plotted vs depth. Temperature data were acquired using the T12 probe by the Department of Water, Land and Biodiversity Conservation at irregular intervals. Uncertainty in temperature is less than the thickness of the line and so is not displayed. Plotted points indicate individual measurements. Conductivities and uncertainties of 24 samples have been measured using the TCS. A weighted harmonic mean has been used to determine the thermal conductivity of the formations traversed. The grey box indicates the standard deviation of the stratigraphy's thermal conductivity. Thermal conductivities are not corrected for *in situ* temperature due to poorly sampled temperature. Mean heat flow has been determined for intervals where temperature and conductivity data are adequately located.
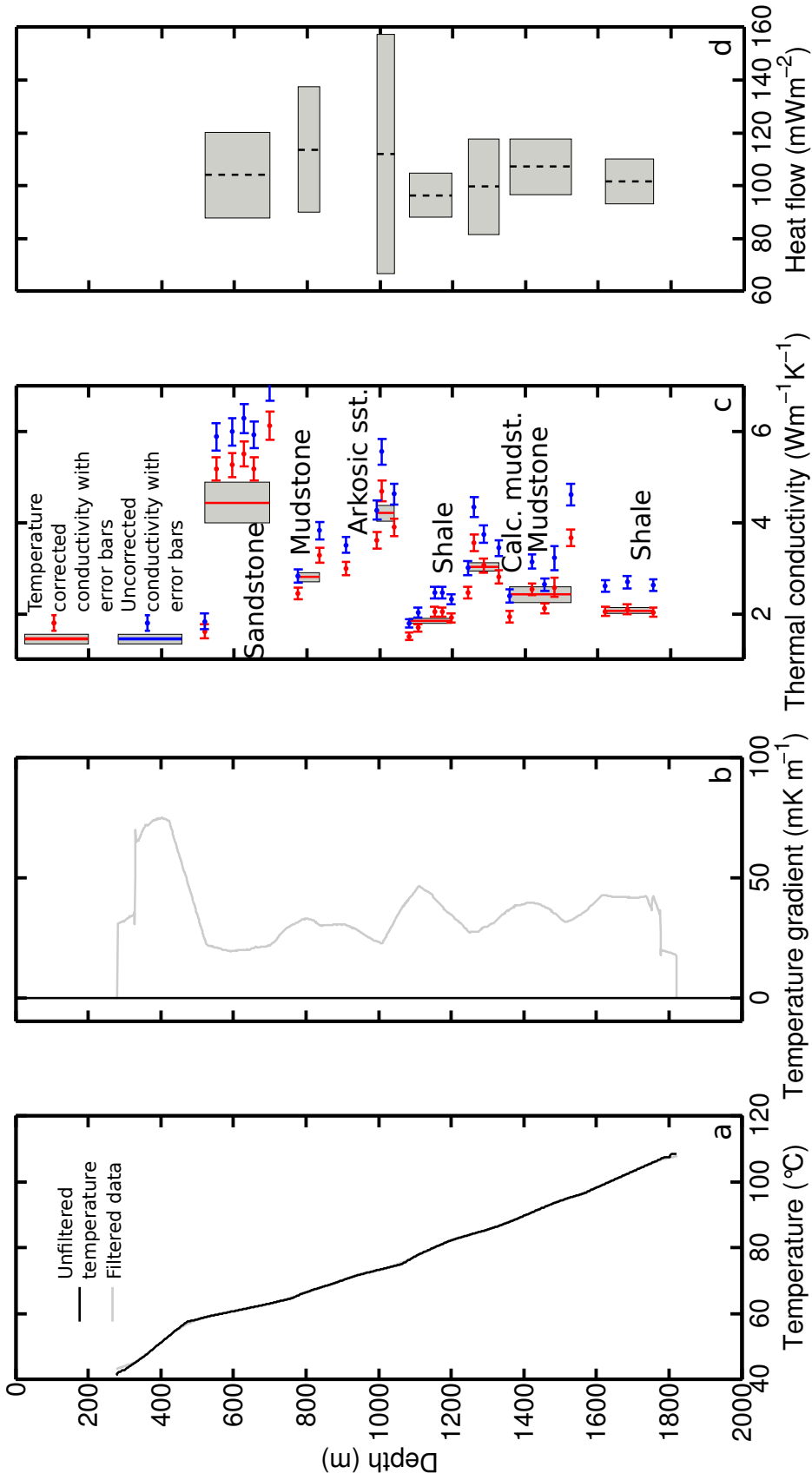
Figure 7: Paralana 1B temperature (a), thermal gradient (b), saturated thermal conductivity (c) and heat flow (d) are plotted vs depth. Temperature data were acquired by Baker Hughes using a Kuster probe with 1 sample per metre. Uncertainties in temperature and thermal gradient are less than the thickness of the line and so are not displayed. The thermal gradient was determined for a given depth by using a window with size of 100 data points. Surface climatic effects are assumed not to apply to this hole as the temperature was only logged from a depth of 300 m, and so the reduced temperature has not been plotted. Conductivities and uncertainties of 29 samples have been determined by Hot Dry Rock Pty Ltd using the divided bar method. Individual conductivity measurements before and after temperature correction are displayed. A weighted harmonic mean has been used to determine the thermal conductivity of the formations traversed. The grey box indicates the standard deviation of the stratigraphy's thermal conductivity. All conductivity measurements are corrected for *in situ* temperature. Mean heat flow has been determined for each stratigraphic package using the product method, taking the harmonic mean of thermal conductivity for the package and using the temperature at the top and bottom of the package to acquire the thermal gradient.
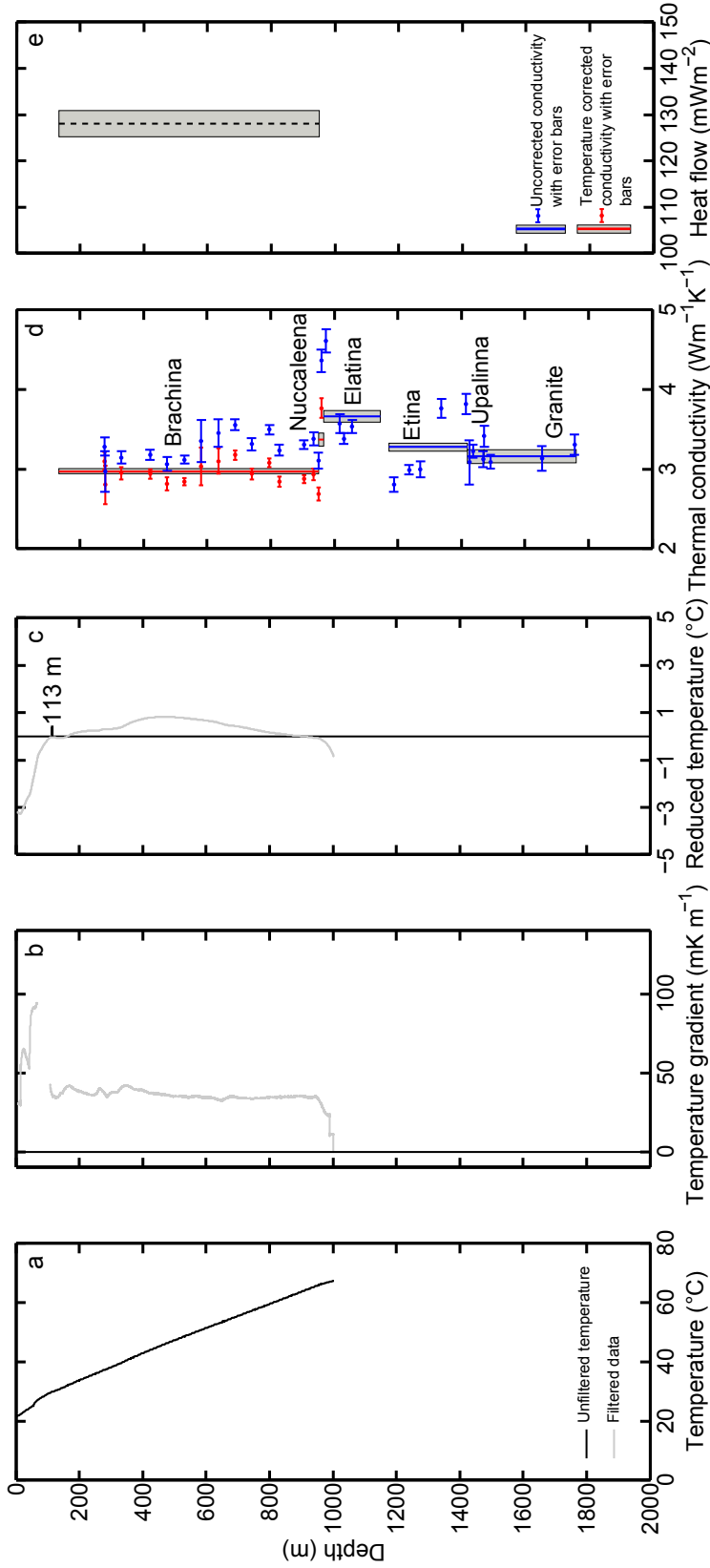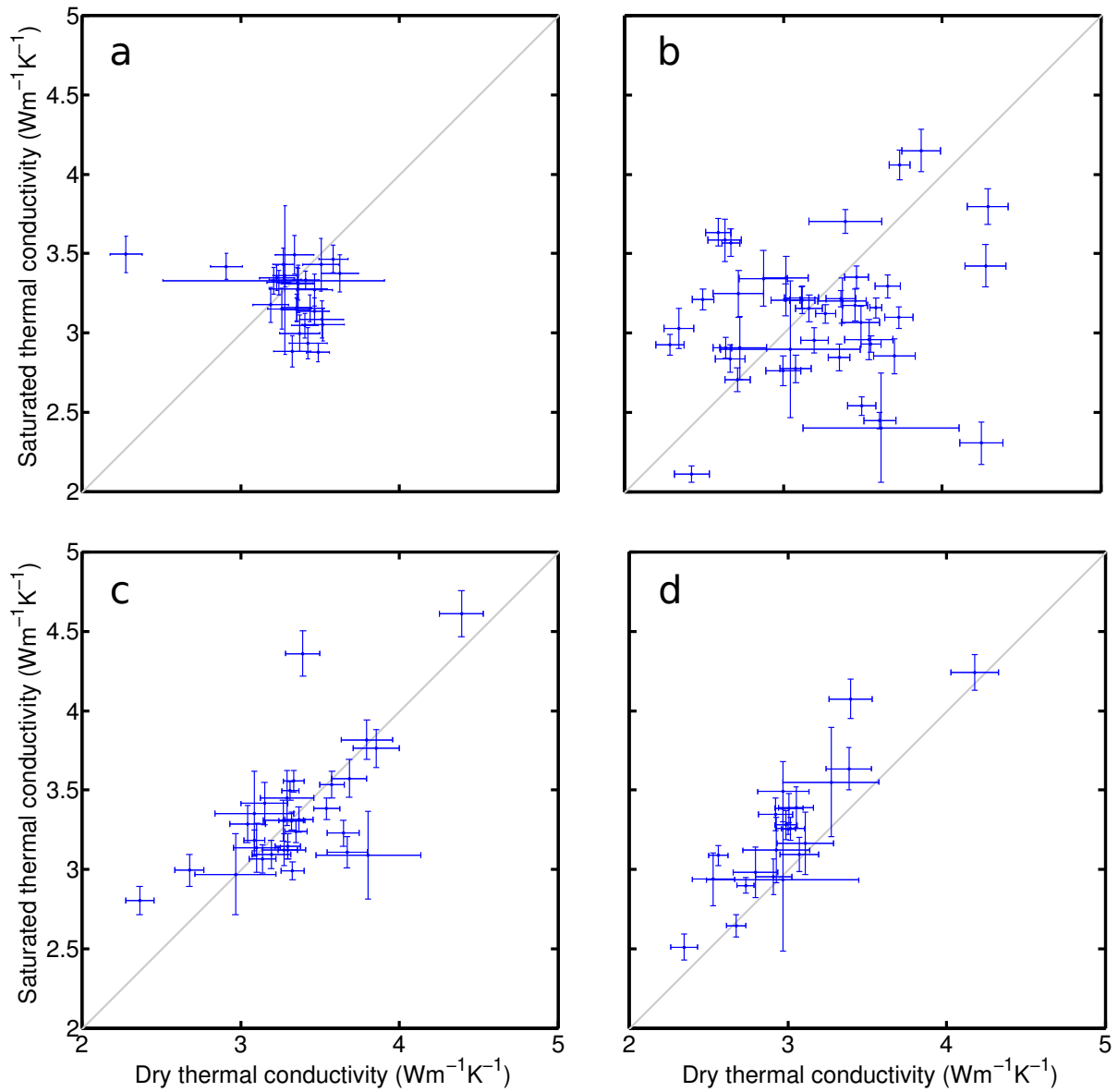
Figure 8: Comparison of dry and saturated thermal conductivity measurements of drill core for Frome 8 (a), 9 (b), 12 (c) and 13(d) samples. Thermal conductivities are not corrected for temperature. A 1 to 1 reference line is depicted in grey.

was measured over several weeks. It is interesting to note that Frome 12 and 13 were measured saturated first, with several months allowed for drying before the dry measurements, while Frome 8 and 9 were measured dry first. Some process may occur during the saturation of core that changes the rock properties sufficiently to deviate from the expected trend. For example, saturation may open fractures, altering the heating dynamics of samples. Cracks may also form a barrier for heat flow when dry but produce a negligible effect when saturated (Walsh & Decker, 1966). While a satisfactory answer cannot be provided here, it is evident that the thermal conductivity of saturated samples in this study does not reproduce the relationships suggested in Somerton (1992). It is also noted that structural factors are unique for varying rock types, creating difficulty in the modelling of thermal conductivity with varying porosity and saturation (Somerton, 1992).

Heat flow

Heat flow estimates using the product method for Frome 8, 9, 12, 13 and Paralana 1B are displayed in Figures 3 through 7. Heat flow for Frome 8 (Figure 3) in the Amberoona Formation in the interval of 100-477 m was estimated to be 84.352 ± 4.520 mW m^{-2}, taken to represent the surface heat flow. Heat flow was estimated for Frome 9 (Figure 4) in the Amberoona Formation in the interval of 92-310 m to be 119.032 ± 5.479 mW/m2, and in the Etina Formation in the interval of 310-493 m to be 90.121 ± 7.552 mW m^{-2}. The surface heat flow of Frome 9 was estimated to be the arithmetic mean of the Amberoona and Etina formations, which is 104.576 ± 4.665 mW m^{-2}. Heat flow was estimated for Frome 12 (Figure 5) in the Brachina Formation in the interval of 134.3-949.8 m to be 128.051 ± 2.817 mW m^{-2}, taken to represent the surface heat flow.

Heat flow was estimated for Frome 13 (Figure 6) in intervals where temperature and thermal conductivity data are adequately located, with seven intervals specified in Fig-

ure 6. Six of these intervals yielded heat flows between 94.162 to 124.853 mW m^{-2}, while one interval yielded a heat flow estimate of 171.510 $\pm$ 16.224 mW m^{-2}. This unusually high value was assumed to be spurious and the result of poorly sampled data. The thermal gradient for this interval is 65.04 mK m^{-1}, estimated using two points at depths of 780 and 903 m. This measurement was not included in the calculation of surface heat flow. The arithmetic mean of the remaining six intervals gave a surface heat flow estimate of 113.726 $\pm$ 16.434 mW m^{-2}.

Heat flow was estimated for Paralana 1B (Figure 7) in seven stratigraphies from ~518-1752 m. The heat flow estimates of the stratigraphies in Paralana 1B range from 96.443 to 113.760 mW m^{-2} and are generally consistent. The mean of each individual heat flow estimate was taken to be the surface heat flow, yielding an estimate of 105.012 $\pm$ 8.410 mW m^{-2}.

Heat flow estimated using the thermal resistance method is displayed in Figure 9, showing heat flows of 84.4 mW m^{-2} for Frome 8, 105.8 mW m^{-2} for Frome 9, 128.1 mW m^{-2} for Frome 12 and 101.9 mW m^{-2} for Paralana 1B.

DISCUSSION

Surface effects

Reduced temperature for drill holes Frome 8, 9 and 12 are displayed in Figures 3 through 5. Depths where reduced temperatures plot above zero indicate regions of temperatures greater than expected from the thermal gradient. This may be due to either local heat generation or a reduction in thermal conductivity (Baillie, 1993). Significant step changes may be indicative of changing lithology. Groundwater flow may introduce advective heat transfer, invalidating the assumption that heat transfer is purely convective. The depth at which the reduced temperature initially transitions from negative to
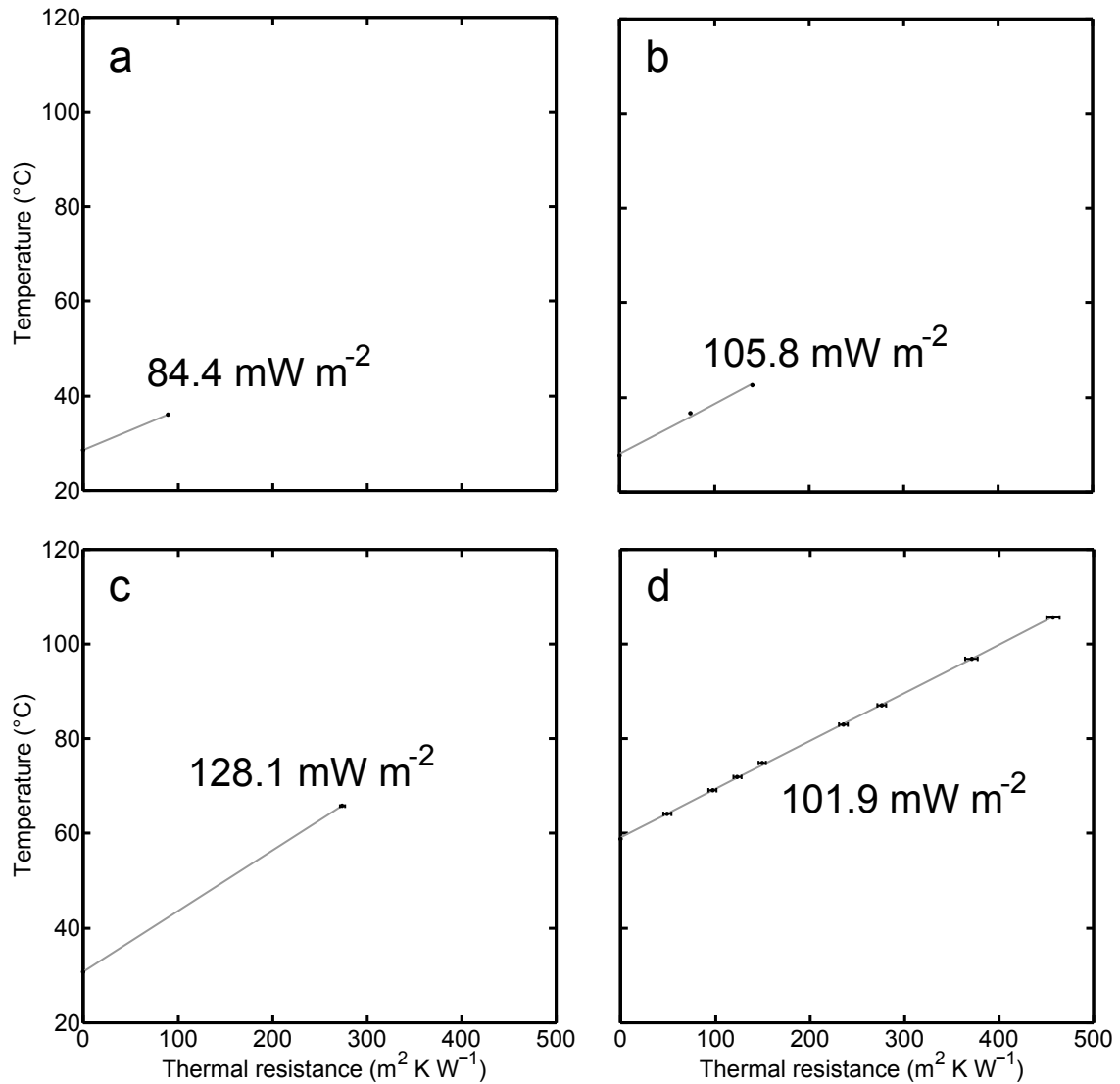
Figure 9: Bullard plots for Frome 8 (a), 9 (b), 12 (c) and Paralana 1B (d). Individual data points indicate the temperature and thermal resistance at the top and bottom of each stratigraphic package or interval. A linear regression line is plotted to estimate the mean heat flow for each hole. Error bars show the uncertainty in thermal resistance. The uncertainty in temperature is smaller than the points and so is not displayed.

positive values is interpreted as the depth where surface effects, such as recent climatic changes (e.g. Jessop, 1990), decay to negligible levels, and where heat transfer is purely convective. Recent glaciation may impact temperature profiles up to depths of 1000 m (Slagstad et al., 2008), however is non-existent in the CP and MPP (Harrison & Dodson, 1994). The depths at which surface climatic effects are negligible are interpreted as $\sim$61 m for Frome 8, $\sim$84 m for Frome 9 and $\sim$113 m for Frome 12.

Other surface effects include topography (e.g. Blackwell et al., 1980), sedimentation/denudation, and refraction. The topography of the CP and MPP is largely parallel, and so topographic effects are considered negligible in this study. Sedimentation rates are minimal (McLaren et al., 2003), and denudation rates are too low to cause any significant steepening of the geotherm (McLaren et al., 2003). Heat flow may be refracted away from zones of low thermal conductivity, for example intrusions, and channeled towards zones of high thermal conductivity in regions of non-parallel stratigraphies (Cull & Beardsmore, 2001). Basement relief and salt domes may perturb heat flow, however the stratigraphy of the Frome and Paralana sites is sub-horizontal and sub-parallel, and so refraction of heat flow is negligible (Cull & Beardsmore, 2001).

Lateral comparison of stratigraphic thermal conductivities

Lateral variations of CP stratigraphies are compared to determine whether using thermal conductivity from a proximal drill hole is a valid proxy for estimating heat flow. To provide a representative comparison, the conductivities are left uncorrected for temperature.

Thermal conductivity of the Amberoona Formation is similar in Frome 8 and 9, located $\sim$50 km apart. Thermal conductivity of the Etina formation in Frome 12 and 13 is similar, however is somewhat lower in Frome 9, which likely indicates lateral variation. The Elatina and Brachina formations show relatively consistent conductivities between

Frome 12 and 13. More data are needed to test the degree of lateral variability in conductivity for CP stratigraphies, however this preliminary study is encouraging for the use of thermal conductivities from neighbouring bore holes to provide an estimate of heat flow.

Chapman et al. (1984) measure lateral variation of thermal conductivity from sedimentary packages within the Uinta Basin, Utah, and conclude that lateral variation is too great to use as a simple proxy for neighbouring bore holes. Chapman et al. (1984) create contour maps of thermal conductivity for each stratigraphic package, allowing more accurate estimates of conductivity for a given location. This exercise was not feasible in this study due to a lack of drill holes, however a future study might expand upon the mean thermal conductivities presented in this study to develop such a map.

Heat flow

The heat flow values from the Frome holes are consistent with other heat flow measurements made in the CP. The mean heat flow in the CP based on existing data and measurements made in this study is 99 mW m^{-2}. The heat flow measured for Paralana 1B is slightly lower than but consistent with Petratherm's estimate of 110 mW m^{-2} (G. Beardsmore pers. comm. 2014). Heat flow values for contiguous stratigraphic packages are generally relatively consistent, indicative of high quality estimates. Heat flow is consistent over the depth of a hole where no advective or convective heat flow exists (Cull & Beardsmore, 2001). The heat flow of Frome 9 in the Amberoona Formation is $\sim$29 mW m^{-2} higher than the Etina formation. While unusual, this discrepancy may be explained by advective heat flow adding or removing heat, however this is unlikely due to the low interconnected porosity of the formations. Shallow radiogenic heat generation may also create this effect, however is also considered unlikely due to sedimentary rocks generally having a low radiogenic concentration. It is worth noting, however, that many

sedimentary-hosted radiogenic deposits lie in this region, including the Honeymoon deposit $\sim$25 km to the east of Frome 8 (Roach et al., 2014).

The heat flow values estimated from thermal resistance (Figure 9) are similar to those estimated from the product method, indicating a reliable estimate. Points on a Bullard plot should produce a straight line for an interval with a purely conductive and steady-state vertical heat flow and negligible internal heat generation. Uncertainties in thermal conductivity and temperature measurements may produce a scatter about the true heat flow. As core samples are assumed to be representative of the thermal conductivity for half the distance to the nearest sample on either side, varying conductivity between these samples is not accounted for, adding to this scatter.

Other possible reasons for non-linear Bullard plots include fluid advection, heat refraction, diagenetic and metamorphic processes, sedimentation and erosion, climatic effects, basement relief, salt domes and steep surface topography. As discussed previously in the section on surface effects these are not considered to significantly impact the Frome and Paralana study areas.

Source of the SAHFA

McLaren et al. (2003) and Neumann et al. (2000) state that the anomalously high heat flow of the Australian Proterozoic terranes results from one or a combination of the following: systematic error bias in the estimation of heat flow, recent tectonic, magmatic and/or hydrologic activity, anomalous mantle heat flow, or anomalous contribution of crustal heat sources. These possibilities are discussed below.

SYSTEMATIC ERROR BIAS OF HEAT FLOW

McLaren et al. (2003) adequately demonstrate that there is no reason for heat flow estimates of a particular tectonic age to suffer a systematic bias. Cull (1982) shows

that 75 % of Australian heat flow data have an error of 15 % or less. While heat flow sites within the SAHFA are concentrated in the vicinity of geothermal and localities with enriched heat producing granites, the distribution of consistently high heat flow observations suggest the SAHFA is indeed a region of pervasive high heat flow. It may be possible that targeting these highs increases the estimate of the magnitude of the SAHFA somewhat, though not enough to account for the anomalous nature of the regional high compared with the global average.

RECENT TECTONIC, MAGMATIC AND HYDROLOGIC ACTIVITY

McLaren et al. (2003) claim that recent tectonic activities are unlikely sources for anomalous heat flow in the SAHFA due to a lack of evidence of recent tectonism. However, significant levels of neotectonism are evident in the Flinders Ranges (Sandiford, 2003) and the MPP (Belperio, 1995), which must be considered as a potential source for elevated heat flow.

The amount of frictional heat generated during fault-slip is controlled by the frictional strength of the fault (d'Alessio et al., 2006). Once generated, heat is transported away from the fault through conductive and advective processes (d'Alessio et al., 2006). For example, a 0.31 °C temperature anomaly was observed at the boundary of the Tohoku-Oki fault 16 months after the 9.0 magnitude March 2011 earthquake off the coast of Japan, corresponding to 27 megajoules per square meter of dissipated energy (Fulton et al., 2013). Fault movement may also transport heat through displacement of geological units, juxtaposing hot material with cold material, leading to a change in heat flow direction from vertical to lateral as heat flows to the colder block (d'Alessio et al., 2006).

The highest MPP heat flow measurement (126 mW m^{-2}; Sass et al., 1976) is located on the bounding escarpment of the upland system (Neumann et al., 2000), though Cull (1982) argues that this measurement is of poor quality. The site is located within several kilometres of the recently rejuvenated Mount Painter escarpment (Sandiford, 2003) and

within 10 km of an active hot spring (McLaren et al., 2006), and so the measurement may not be representative of conductive heat flow. Fault offsets suggest there has been significant recent displacement on the Paralana and associated faults (Sandiford, 2003). Belperio (1995) reports that the Mt Babbage Inlier basement rocks have been thrust over collovium that may be as young as Holocene. The uplift of the Flinders Ranges began during the Late Miocene and continued into the Quaternary (Callen & Tedford, 1976). These observations imply that late Neogene tectonism has contributed significantly to present topographic relief in the northern Flinders Ranges (Sandiford, 2003). The CP and the Gawler Craton are more stable and largely unaffected by recent tectonism (e.g. Sandiford, 2003).

The San Andreas fault is associated with high heat flows in excess of 74 mW m^{-2} (Sass et al., 1997) and an average slip rate of 21-26 mm/yr (Titus et al., 2006). In comparison, slip rates of faults in South Australia are estimated to be significantly lower, from 0.020-0.051 mm per year (Quigley et al., 2006). It is apparent that anomalous heat flow extends well beyond regions of recent tectonic activity and that fault movement is minimal compared to seismically active regions where elevated heat flow is associated with faults, indicating that frictional heating is likely not a significant factor for the SAHFA.

Magmatic activity is unlikely to impact the SAHFA as the closest active magmatic province is at Mount Gambier to the south east (Cull, 1982). There is no evidence of magmatism in the SAHFA since early Phanerozoic (McLaren et al., 2003). The denudation rates of the SAHFA are too low to cause significant steepening of the geotherm (McLaren et al., 2003). Hydrologic activity is low in the region (McLaren et al., 2003). Areas of fluid recharge are generally larger than areas of discharge (e.g. Cook, 2003), i.e. zones with cold meteoric water flowing into a region are more likely to be sampled for heat flow than zones with hot water heated by deep rock flowing out. As a result,

even if hydrologic effects were a significant impact in the SAHFA, it is expected that the effects would bias the heat flow to be lower. It is therefore unlikely that the elevated heat flow of the SAHFA is due to hydrologic bias.

ANOMALOUS MANTLE HEAT FLOW SOURCE

Previous analyses of seismic data show high P and S wave velocities in the central Australian Proterozoic terranes, suggesting that they have the thickest crust in the Australian continent (e.g. Drummond, 1988), and a relatively cool and thick lithosphere (Kennett & van der Hilst, 1996). The Proterozoic upper lithospheric mantle of eastern Australia, where elevated heat flow is attributed to deep mantle sources (Goutorbe et al., 2008), is ~200 °C hotter than in the SAHFA. Neumann et al. (2000) have noted that the temperature of the SAHFA at 40 km depth would be over 800 °C, yielding significantly slower upper mantle velocities than those shown by Zielhaus & van der Hilst (1996), if the heat flow was due solely to anomalous mantle contributions.

More recent seismic data support these observations. Higher seismic velocities beneath cratonic regions in South Australia compared to the central and eastern Tasmanides in southeastern Australia (Rawlinson et al., 2014), a high velocity zone beneath the CP (e.g. Fishwick & Rawlinson, 2012; Rawlinson et al., 2014) and significantly faster lithospheric S and P wave velocities in the SAHFA than southeastern Australia at 100, 150 and 200 km depth (Rawlinson et al., 2011; Kennett et al., 2013; Rawlinson et al., 2014) are suggestive of a cooler, thicker lithosphere. Seismic velocities from the AuSREM model suggest a significantly thicker for the SAHFA (~200 km) compared to southeastern Australia (~90 km; Kennett et al., 2013). While absolute magnitudes of deep seismic data may be unreliable and the seismic lithosphere-asthenosphere boundary (LAB) may be different to the thermal LAB (Artemieva, 2009), the relative magnitudes are accurate and consistently suggest significantly cooler mantle-lithosphere temperatures in the SAHFA compared to southeastern Australia.

To demonstrate how heat flow and crustal heat generation affect lithospheric thickness, three steady-state geotherms are computed using the model developed in Hasterok & Chapman (2011) in Figure 10. Temperature at depth is computed by the equation:

$$T = T_s + \frac{q_s}{\lambda}\Delta z - \frac{A}{2\lambda}\Delta z^2, \tag{10}$$

where T_s is the surface temperature, q_s is the surface heat flow, A is heat generation and Δz is the layer thickness. Geotherms are calibrated by Hasterok & Chapman (2011) using surface heat generation, elevation and xenoliths.

As discussed by Hasterok & Chapman (2011), temperatures are highly sensitive to small variations in upper crustal heat generation, therefore only upper crustal heat generation is varied between scenarios. Geotherms computed using constant heat generation within the upper crustal layer rather than the commonly used exponential decreasing heat generation layer as highly variable heat generation is observed in exposed crustal sections and deep boreholes, invalidating the assumption of exponential heat generation.

Surface heat flow and upper crustal heat generation are varied to compute three geotherms. A depleted lower crust (0.4 μW m^{-3}) and a low mantle heat generation (0.02 μW m^{-3}) are assumed for all geotherms based on the assumptions of Hasterok & Chapman (2011). Geotherm 1 (Figure 10) is representative of a globally average Proterozoic terrane, and computes with a lithospheric thickness of 187.9 km. Geotherm 2 is representative of a region with the heat flow of the SAHFA and moderate shallow crustal heat generation of 1.495 μW m^{-3}, and computes with a lithospheric thickness of 45.6 km. Geotherm 1 and 2 represent a standard family of geotherms. Geotherm 3 is representative of the SAHFA, using a shallow crustal heat generation of 4.14 μW m^{-3}, following from the observations of Neumann et al. (2000).

The lithospheric thickness of geotherm 2 is inconsistent with deep seismic data showing a much deeper LAB at ∼200 km. Geotherm 3, however, is consistent with a thick
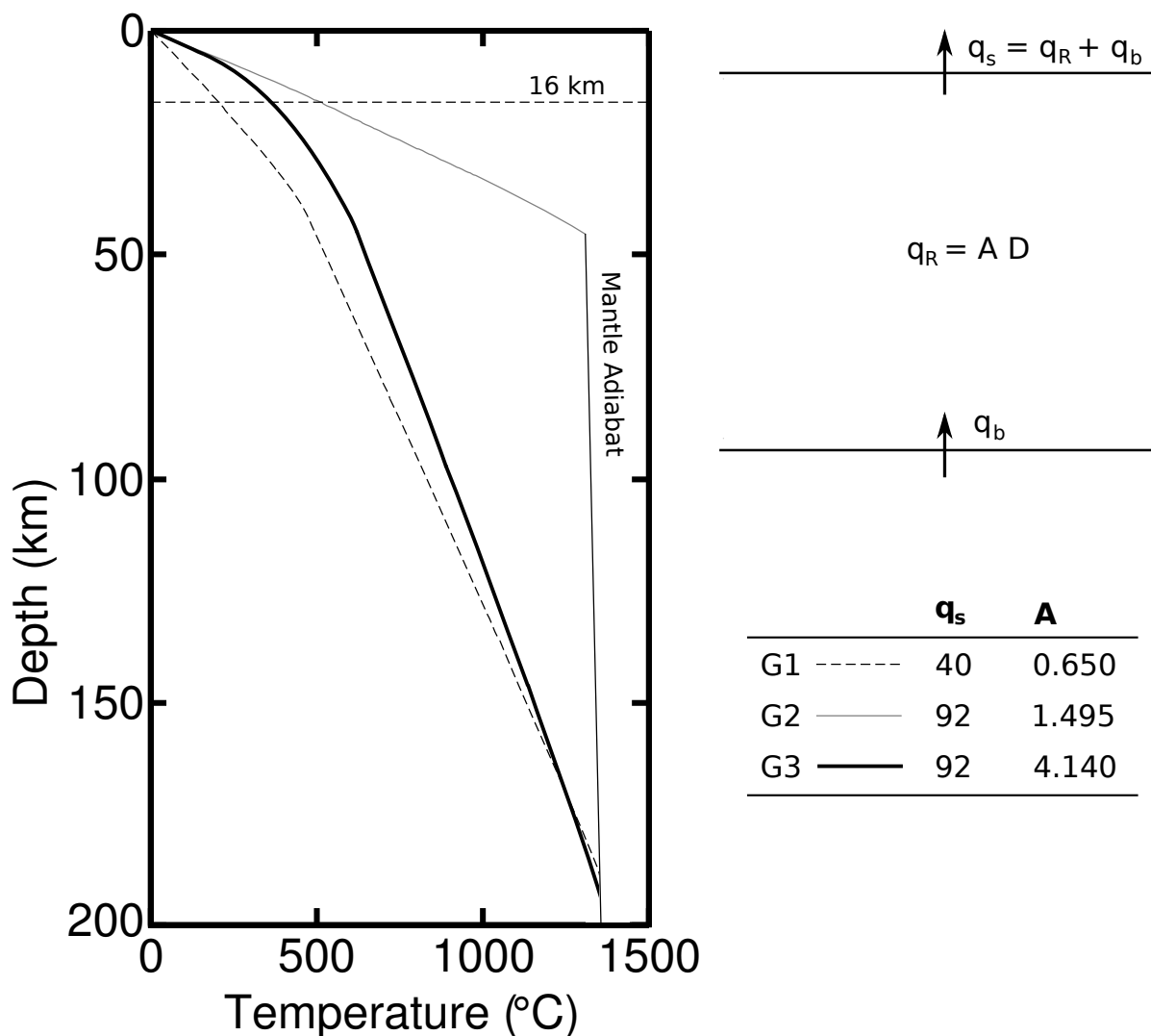
Figure 10: Geotherms illustrating the effect of mantle dominant or upper crustal heat generation dominant contributions to surface heat flow. All geotherms assume an upper crustal thickness of 16 km, a lower crustal heat generation of 0.4 μW m^{-3} and a lithospheric mantle heat generation of 0.02 μW m^{-3}. The point at which each geotherm intersects the adiabatic geotherm is interpreted as LAB for each scenario. The parameters used for each geotherm are depicted in the figure. q_s, surface heat flow, is in mW m^{-2} and A, upper crustal heat generation, is in μW m^{-3}. Top right diagram demonstrates that surface heat flow is the sum of mantle heat flow and heat generated in the crust.

lithosphere, supporting the hypothesis for a shallow crustal heat generation source of the SAHFA.

ANOMALOUS SHALLOW CRUSTAL HEAT FLOW SOURCE

Reiter (2008) demonstrate that the thermal source of anomalies may be estimated from the lateral variation of heat flow. Short wavelength variations in heat flow suggest upper crustal thermal sources, while long wavelength variations in heat flow suggest deeper mantle thermal sources. The heat flow of the San Juan volcanic field, southwestern Colorado, has a relatively large half width of 50-100 km and is attributed to a deep magma plume at ∼100-35 km depth (Reiter & Clarkson, 1983). The relatively short wavelength variations of heat flow in northern Colorado are attributed to a radiogenically enriched 20-30 km thick granite layer in the upper crust (Decker, 1995). Rolandone et al. (2002) attribute small-scale lateral heat flow variations in the Flin Flon-Snow Lake Belt, USA, to changes of heat generation in the upper crust. Here heat flow varies from 51 mW m^{-2} to 37 mW m^{-2} within 15 km.

Heat flow values observed in this study are added to the existing Australian dataset (Figure 11). The original dataset is compared to the dataset including new additions in Figure 12. From Frome 8 to Frome 12, a distance of ∼50 km, surface heat flow increases from 84.352 ± 4.520 mW m^{-2} to 128.051 ± 2.817. These short lateral variations in heat flow are consistent with other regions of shallow crustal sourced heat flow as outlined above, providing strong evidence for an upper crustal radiogenic source.

McLaren et al. (2003) estimate that crustal sources contribute >70 mW m^{-2} in some parts of the SAHFA, consistent with the estimate for the MPP of >80 mW m^{-2} by McLaren et al. (2006). Seismic profiling reveals that granites and granite gneisses comprise a large part of the Australian Proterozoic terranes (Drummond et al., 1998). Normalised heat generation of igneous rocks in central Australian Proterozoic terranes averages 4.6 μW m^{-3} (Wyborn et al., 1998), 1.8 times greater than globally aver-
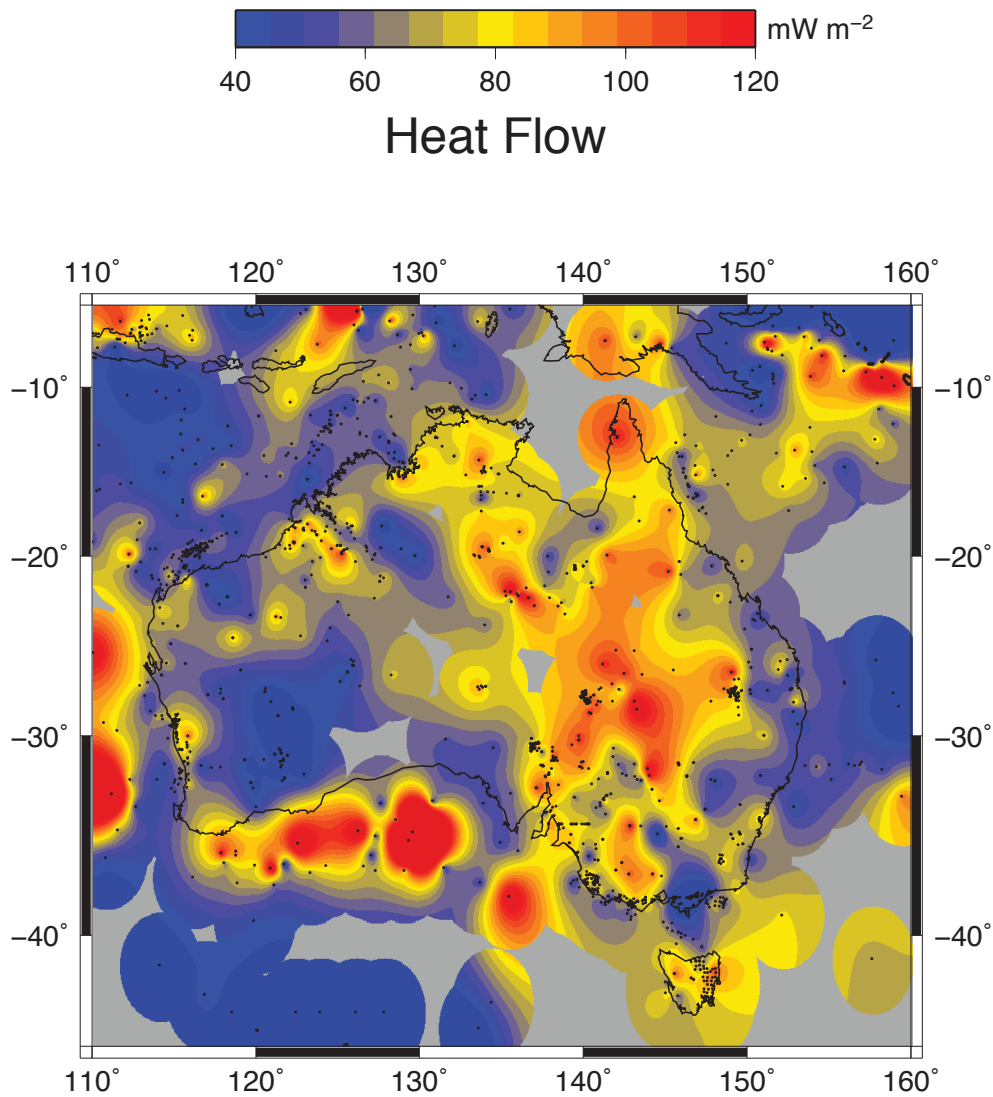
Figure 11: Heat flow of Australia interpolated from existing data (D. Hasterok pers. comm. 2014) and measurements made in this study with a masking radius of 250 km. Data is plotted using GMT (Wessel et al., 2013).
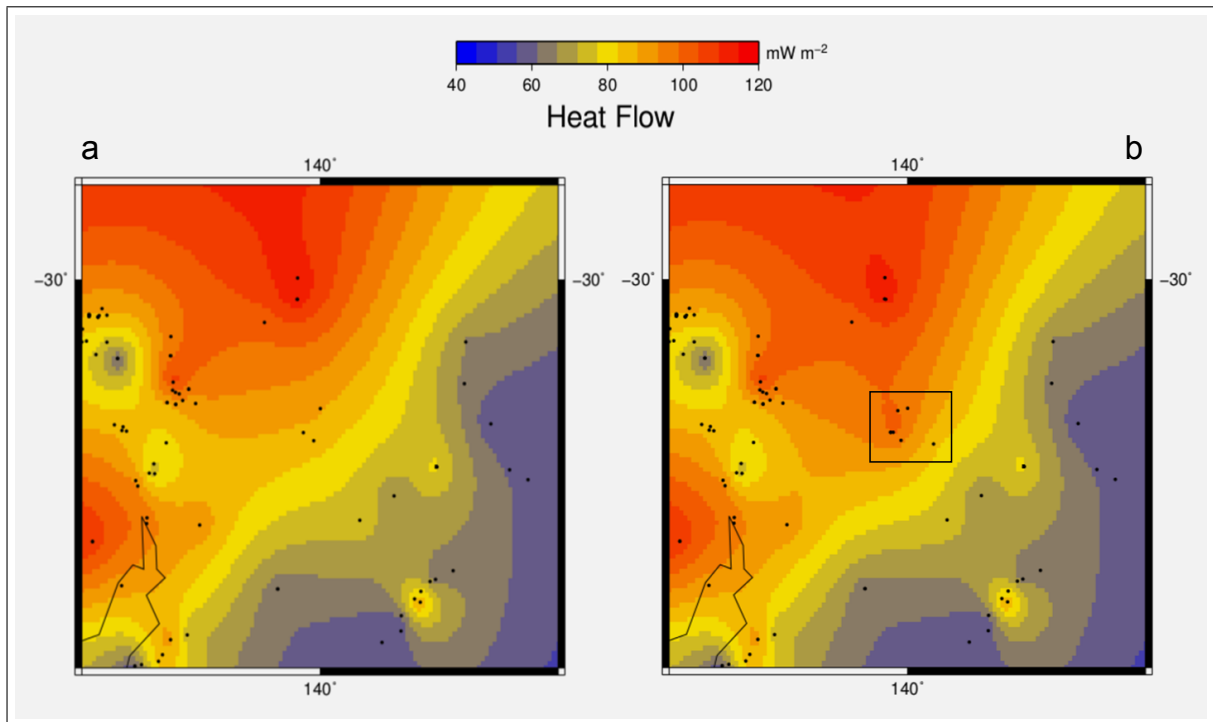
Figure 12: Original heat flow dataset of Australia (a) interpolated from existing data (D. Hasterok pers. comm. 2014), and the updated heat flow dataset (b) with measurements made in this study with a masking radius of 250 km. Plots are zoomed on South Australia, with the box indicating the CP study area. Data are plotted using GMT (Wessel et al., 2013).

age granite (Haenel et al., 1988). Mean heat generation in the MPP is 16 μWm^{-3}, over three times the global upper crustal mean (e.g. Neumann et al., 2000; McLaren et al., 2003; McLaren et al., 2006). The SAHFA hosts significant radiogenic deposits, notably the giant Olympic Damn IOCG $\pm$ U deposit in the eastern Gawler Craton. Neumann et al. (2000) use a surface heat generation dataset of ~2650 samples to show that the SAHFA is strongly characterised by high heat generation.

Voluminous suites of igneous rock are present near the surface in the CP, notably the granites and Benagerie Ridge Volcanics at depths of ~1500 m depth in the Frome study area, and the intrusives at ~3400 m in the Paralana study area, which provide potential sources of radiogenic elements. The Mesoproterozoic granites and gneisses of the MPP

have a mean heat generation of 9.9 μWm^{-3} normalised by area (Neumann et al., 2000). The ca. 1556 Ma Yerila Granite (Neumann, 2001) of the MPP has an exceptionally high heat generation of 61.8 μW m^{-3} (Kromkhun & Foden, 2007).

Geothermal energy potential

The SAHFA is an unconventional geothermal resource, often termed a Hot Dry Rock (HDR) or Enhanced Geothermal System (EGS), consisting of hot rocks with low permeability (e.g. Duchane & Brown, 2002; Tester, 2006). There are three requirements for a geothermal system to be commercially exploitable; high temperatures at shallow depths, high volume of fluids and high permeability. Depending on the design of goethermal power plant, temperatures of $\sim$60-200 °C are desirable. If one or more of these requirements are not satisfied, they must be enhanced. Fluid volume and permeability may be stimulated through hydraulic fracturing (e.g. Brown et al., 2012; Legarth et al., 2005) and enhanced fluid flow techniques.

The Frome drill holes in the CP demonstrate a high geothermal potential through high temperature gradients, with temperatures of 60 °C at $\sim$810 m depth, and 200 °C at $\sim$6557 m depth. While 6557 m is too deep to drill economically, 810 m is accessible with conventional drilling techniques, indicating that this geothermal resource can be economically developed. Sedimentary cover is up to 1800 m thick in some locations and shown to have an insulating effect on heat (e.g. Abul Khair et al., 2015). Thermal conductivity decreases with increasing heat, and thus hot sedimentary formations become more effective at trapping heat in regions of high heat flow. The Paralana study area in the MPP also has a high geothermal gradient with temperatures of 60 °C at $\sim$565 m depth, and 200 °C at $\sim$4415 m depth, with sedimentary cover up to 4000 m thick. Drilling through 4000 m of sediment can be achieved with conventional drilling techniques, and while it may not be economical to drill geothermal exploration wells this

deep, production wells are likely to be economic at these depths. Future studies should aim to compare these depths with the estimated costs of drilling and estimated rate of return from the geothermal resource to determine the true viability of developing these resources.

Rock permeability is strongly influenced by fracture network characteristics (Abul Khair et al., 2012). Granites generally have low permeabilities (Brace et al., 1968), though pre-existing joints and fractures in SAHFA granites may be re-opened through hydraulic stimulation, enhancing permeability by several orders of magnitude (Chopra & Holgate, 2003).

Several projects are currently operating in the SAHFA. Petratherm's Paralana project demonstrates a total estimated recoverable resource of 38,000 PJ, with 9,300 PJ in the target zone for initial development of 3,500-4,000 m (Petratherm, 2011). Geothermal Resources Frome project demonstrates a total estimated recoverable resource of 84,000 PJ, with electricity generating potential of 460,000 GWh (Geothermal-Resources, 2009).

At present, the most significant barrier to the development of geothermal resources in South Australia is the distance from the electrical grid and energy market. If these technical issues can be bridged through a combination of supplying power to South Australia's large number of mine and hydrocarbon facilities and new energy transport infrastructure, geothermal energy has significant potential into the future.

CONCLUSIONS

New surface heat flow estimates from five drill holes were made in the SAHFA from temperature profiles and thermal conductivities measured in this study and provided by the Department of State Development and Petratherm. The mean heat flow in the Curnamona Province based on existing data and measurements made in this study is 99 mW m^{-2}. The following results and observations from this study support the hypothesis of a shallow crustal radiogenic source for the SAHFA:

- A lack of significant recent tectonic, magmatic and hydrologic activity across the heat flow anomaly.

- Analysis of previous seismic work suggests a significantly cooler and thicker lithosphere in the SAHFA compared to regions with anomalous mantle heat flow.

- Computed geotherms successfully recreate the estimated lithospheric thickness of the SAHFA using parameters of observed surface heat flow and shallow crustal heat generation.

- Short wavelength lateral variations of heat flow in the Curnamona Province from drill holes measured here and in previous studies, consistent with other global regions of crustal sourced heat flow.

- Heat generation of basement rock within the SAHFA is exceptionally high, primarily hosted in Mesoproterozoic granites, and is up to 61.8 µW m^{-3} in the Mount Painter Province.

Thermal conductivity of stratigraphic packages within the Curnamona Province was found to exhibit lateral variation. Creating a contour map of thermal conductivities will allow drill holes without thermal conductivity data to be utilised for heat flow estimates, using only temperature profiles. The new data are consistent with previous measurements of high surface heat flow within the Curnamona Province, where high

temperatures at shallow depths and thermally insulating sedimentary cover provide an attractive target for Enhanced Geothermal Systems exploration.

ACKNOWLEDGMENTS

REFERENCES

Abul Khair, H., Cooke, D., King, R., Hand, M. & Tingay, M. (2012). Preliminary workflow for sub-surface fracture mapping using 3D seismic surveys: A case study from the Cooper Basin, South Australia, *Geothermal Research Council Transactions* **36**: 339–350.

Abul Khair, H. H., Cooke, D. & Hand, M. (2015). Seismic mapping and geochemical analyses of faults within deep hot granites, a workflow for enhanced geothermal system projects, *Geothermics* **53**: 46–56.

Anand, J., Somerton, W. H. & Gomaa, E. (1973). Predicting thermal conductivities of formations from other known properties, *Society of Petroleum Engineers Journal* **13**: 267–273.

Armit, R. J., Ailleres, L., Betts, P. G., Schaefer, B. F. & Blaikie, T. N. (2014). High-heat geodynamic setting during the Palaeozoic evolution of the Mount Painter Province, SA, Australia: evidence from combined field structural geology and potential-field inversions, *Geophysical Journal International* **199**: 253–275.

Artemieva, I. (2009). The continental lithosphere: Reconciling thermal, seismic, and petrologic data, *Lithos* **109**: 23–46.

Baillie, P. W. (1993). Investigations into gas of possible geothermal origin and Smithton, *Technical report*, Division of Mines.

Balandin, A. A. (2008). Superior thermal conductivity of single-layer graphene, *Nano Letters* **8**: 902–907.

Balco, G. & Stone, J. O. (2003). Measuring the density of rock, sand, till, etc. UW Cosmogenic Nuclide Laboratory, methods and procedures. http://depts.washington.edu/cosmolab/chem.html.

Balling, N., Kristiansen, J. I., Breiner, N., Poulsen, K. D., Rasmussed, R. & Saxov, S. (1981). Geothermal measurements and subsurface temperature modelling in Denmark, *Technical report*, Department of Geology, Aarhus University. ISSN 0105-824X.

Belperio, A. (1995). *The Geology of South Australia, Volume 2, The Phanerozoic*, Geological Survey of South Australia Bulletin 54, chapter Quaternary, pp. 219–281.

Bevington, P. R. (1969). *Data reduction and error analysis for the physical sciences*, McGraw Hill Book Co., Inc., New York.

Blackwell, D. D. & Spafford, R. E. (1987). *Methods of Exploration Physics*, Academic Press, New York, chapter Experimental methods in continental heat flow, pp. 189–226.

Blackwell, D. D., Steele, J. L. & Brott, C. A. (1980). The terrain effect on terrestrial heat flow, *Journal of Geophysical Research* **85**: 4,757–4,772.

Bowker, C. (2013). Performance and quality control study of the TCS optical scanning instrument. South Australian Centre for Geothermal Energy Research (SACGER), The University of Adelaide.

Brace, W. F., Walsh, J. B. & Frangos, W. T. (1968). Permeability of granite under high pressure, *Journal of Geophysical Research* **73**: 2,225–2,236.

Brown, D. W., Duchane, D. V., Heiken, G. & Hriscu, H. T. (2012). *Mining the Earth's Heat: Hot Dry Rock Geothermal Energy*, Springer-Verlag Berlin Heidelberg.

Bullard, E. C. (1939). Heat flow in South Africa, *Proceedings of the Royal Society of London, A* **173**: 428–450.

Callen, R. A. & Tedford, R. H. (1976). New late Cainozoic rock units and depositional environments, Lake Frome Area, South Australia, *Transactions of the Royal Society of South Australia* **100**: 125–167.

Carslaw, H. & Jaeger, J. C. (1947). *Conduction of Heat in Solids*, Clarendon Press, Oxford.

Chapman, D., Keho, T., Bauer, M. & Picard, M. (1984). Heat flow in the Uinta Basin determined from bottom hole temperature (BHT) data, *Geophysics* **49**: 453–466.

Chopra, P. & Holgate, F. (2003). Australias first hot dry rock geothermal energy extraction project is up and running in granite beneath the Cooper Basin, NE South Australia, *Geoscience Australia Record* **14**: 43–45.

Coats, R. P. & Blissett, A. H. (1971). Regional and economic geology of the Mount Painter Province, *Geological Survey of South Australia Bulletin* **43**.

Conor, C. H. H. & Preiss, W. V. (2008). Understanding the 1720-1640 Ma Palaeoproterozoic Willyama Supergroup, Curnamona Province, Southeastern Australia: implications for tectonics, basin evolution and ore genesis, *Precambrian Research* **166**: 297–317.

Cook, P. G. (2003). A guide to regional groundwater flow in fractured rock aquifers, *Technical report*, Adelaide: CSIRO Land and Water.

Cull, J. & Beardsmore, G. (2001). *Crustal Heat Flow: A guide to measurement and modelling*, Cambridge University Press.

Cull, J. P. (1982). An appraisal of Australian heat-flow data. BMR, *Journal of Australian Geology & Geophysics* **7**: 11–21.

d'Alessio, M. A., Williams, C. F. & Burgmann, R. (2006). Frictional strength heterogeneity and surface heat flow: Implications for the strength of the creeping San Andreas fault, *Journal of Geophysical Research* **111**: B05410.

Decker, E. R. (1995). Thermal regimes of teh Southern Rocky Mountains and Wyoming Basin in Colorado and Wyoming in the United States, *Tectonophysics* **244**: 85–106.

Deming, D. & Chapman, D. S. (1988a). Heat Flow in the Utah-Wyoming Thrust Belt from analysis of bottom-hole temperature data measured in oil and gas wells, *Journal of Geophysical Research* **93**: 13,657–13,672.

Deming, D. & Chapman, D. S. (1988b). Inversion of bottom-hole temperature data: The Pineview field, Utah-Wyoming thrust belt, *Geophysics* **53**: 707–720.

Demongodin, L., Pinoteaue, B., Vasseur, G. & Gable, R. (1991). Thermal conductivity and well logs: a case study in the Paris Basin, *Geophysical Journal International* **105**: 675–691.

Drummond, B., Goleby, B., Goncharov, A., Wyborn, A., Collins, C. & MacCready, T. (1998). Crustal-scale structures in the Proterozoic Mount Isa inlier of north Australia: their seismic response and influence on mineralisation, *Tectonophysics* **288**: 43–56.

Drummond, B. J. (1988). A review of crust/upper mantle structure in Precambrian areas of Australia and implications for Precambrian crustal evolution, *Precambrian Research* **40/41**: 101–116.

Duchane, D. & Brown, D. (2002). Hot dry rock (HDR) geothermal energy research and development at Fenton Hill, New Mexico, *Geo-Heat Centre Q. Bulletin* **23**: 13–19.

Fishwick, S. & Rawlinson, N. (2012). 3-D structure of the Australian lithosphere from evolving seismic datasets, *Australian Journal of Earth Sciences* **59**: 809–826.

Fulton, P. M., Brodsky, E. E., Kano, Y., Mori, J., Chester, F., Ishikawa, T., Harris, R. N., Lin, W., Eguchi, N. & Tockzko, S. (2013). Low coseismic friction on the Tohoku-Oki Fault determined from temperature measurements, *Science* **342**: 1,214–1,217.

Funnell, R., Chapman, D., Allis, R. & Armstrong, P. (1996). Thermal state of the Taranaki Basin, New Zealand, *Journal of Geophysical Research* **101**: 25,197–25,215.

Gallagher, K. (1990). Some strategies for estimating present day heat flow from exploration wells, with examples, *Exploration Geophysics* **21**: 145–159.

Geothermal-Resources (2009). Frome Project - Statement of Estimated Geothermal Resources, *Technical report*. ASX/Media Release.

Gilliam, T. M. & Morgan, I. L. (1987). Shale: Measurement of thermal properties, *Technical report*, Oak Ridge National Laboratory. ORNL/TM-10499.

Goutorbe, B., Lucazeau, F. & Bonneville, A. (2008). Surface heat flow and the mantle contribution on the margins of Australia, *Geochemistry Geophysics Geosystems* **9**.

Haenel, R., Rybach, L. & Stegena, L. (1988). *Handbook of Terrestrial Heat-flow Density Determination: with Guidelines and Recommendations of the International Heat Flow Commission*, Kluwer Academic Publishers, Dordrecht.

Harrison, S. & Dodson, J. (1994). *Global Climates: Since the Last Glacial Maximum*, University of Minnesota Press, chapter Climates of Australia and New Guinea since 18,000 yr B.P., pp. 265–293.

Hasterok, D. & Chapman, D. (2011). Heat production and geotherms for the continental lithosphere, *Earth Planet. Sci. Lett.* **307**: 59–70.

Jessop, A. M. (1990). *Thermal Geophysics*, Developments in Solid Earth Geophysics, Elsevier, Amsterdam.

Kennett, B., Fichtner, A., Fishwick, S. & Yoshizawa, K. (2013). Australian Seismological Reference Model (AuSREM): Mantle component, *Geophysical Journal International* **192**: 871–887.

Kennett, B. L. N. & van der Hilst, R. D. (1996). Using a synthetic continental array in Australia to study the Earth's interior, *Journal of Physics of the Earth* **44**: 669–674.

Korsch, R. J. (2010). Geological interpretation of deep seismic reflection and magnetotelluric line 08GA-OM1: Gawler Craton-Officer Basin-Musgrave Province-Amadeus Basin (GOMA), *Technical report*, South Australia and Northern Territory Geoscience Australia.

Kromkhun, K. & Foden, J. (2007). Some characteristics and a possible genesis of extremely high heat producing Mesoproterozoic granites from Mount Painter Province, South Australia. Origin of Granitic Rocks 6th International Hutton Symposium. University of Stellenbosch, South Africa.

Kromkhun, K., Foden, J., Hore, S. & Baines, G. (2013). Geochronology and Hf isotopes of the bimodal mafic-felsic high heat producing igneous suite from Mt Painter Province, South Australia, *Gondwana Research* **24**: 1,067–1,079.

Lam, H. L., Jones, F. W. & Lambert, C. (1982). Geothermal gradients in the Hinton area of west-central Alberta, *Canadian Journal of Earth Sciences* **19**: 755–766.

Lee, Y. & Deming, D. (1998). Evaluation of thermal conductivity temperature corrections applied in terrestrial heat flow studies, *Journal of Geophysical Research: Solid Earth* **103**: 2,447–2,454.

Legarth, B., Huenges, E. & Zimmermann, G. (2005). Hydraulic fracturing in a sedimentary geothermal reservoir: results and implications, *International Journal of Rock Mechanics and Mining Science* **42**: 1,028–1,041.

Matthews, C. (2009). Geothermal energy prospectivity of the Torrens Hinge Zone: evidence from new heat flow data, *Exploration Geophysics* **40**: 288–300.

Matthews, C. & Beardsmore, G. (2007). New heat flow data from South-Eastern South Australia, *Exploration Geophysics* **38**: 260–269.

McLaren, S., Sandiford, M., Hand, M., Neumann, N., Wyborn, L. & Bastrakova, I. (2003). The hot southern continent: heat flow and heat production in Australian Proterozoic terranes, *Geological Society of Australia Special Publication* **22**: 151–161.

McLaren, S., Sandiford, M., Powell, R., Neumann, N. & Woodhead, J. (2006). Palaeozoic intraplate crustal anatexis in the Mount Painter Province, South Australia: Timing, Thermal budgets and the role of crustal heat production, *Journal of Petrology* **47**: 2,281–2,302.

Midttømme, K. K. & Roaldset, E. (1999). Thermal conductivity of sedimentary rocks: uncertainties in measurement and modelling, *Geological Society special publication* **158**: 45–60.

Neumann, N. (2001). Geochemical and isotopic characteristics of South Australian Proterozoic granites: implications for the origin and evolution of high heat-producing terrains. Ph.D. Thesis, University of Adelaide.

Neumann, N., Sandiford, M. & Foden, J. (2000). Regional geochemistry and continental heat flow: implications for the origin of the South Australian heat flow anomaly, *Earth and Planetary Science Letters* **183**: 107–120.

Petratherm (2011). Paralana Resource Statement. http://www.petratherm.com.au/reports.html.

Popov, A. M., Kiselev, A. I. & Mordvinova, V. V. (1999). Geodynamical interpretation of crustal and upper mantle electrical conductivity anomalies in Sayan-Baikal province, *Earth Planets Space* **51**: 1,079–1,089.

Popov, Y. A., Berezin, V. V., Semionov, V. G. & Korosteliov, V. M. (1985). Complex detailed investigations of the thermal properties of rocks on the basis of a moving point source, *Izvestiya, Earth Physics* **21**(1): 64–70.

Popov, Y. A., Pribnow, D. F. C., Sass, J. H., Williams, C. F. & Burkhardt, H. (1999). Characterization of rock thermal conductivity by high-resolution optical scanning, *Geothermics* **28**: 253–276.

Preiss, W., Korsch, R., Blewett, R., Fomin, T., Cowley, W., Neumann, N. & Meixer, A. (2010). Geological interpretation of deep seismic reflection line 09GA-CG1: the Curnamona Province-Gawler Craton Link Line, South Australia.

Preiss, W. V. (1990). A stratigraphic and tectonic overview of the Adelaide Geosyncline, South Australia, *The Evolution of a Late Precambrian–Early Palaeozoic Rift Complex: The Adelaide Geosyncline, Geological Society of Australia, Special Publication* **16**: 1–33.

Quigley, M. C., Cupper, M. L. & Sandiford, M. (2006). Quaternary faults of south-central Australia: palaeoseismicity, slip rates and origin, *Australian Journal of Earth Sciences* **53**: 285–301.

Ramires, M. L. V., Nieto de Castro, C. A., Nagasaka, Y., Nagashima, A., Assael, M. J. & Wakeham, W. A. (1995). Standard reference data for the thermal conductivity of water, *Journal of Physical and Chemical Reference Data* **24**: 1,377–1,381.

Rawlinson, N., Kennett, B. L. N., Vanacore, E., Glen, R. A. & Fishwick, S. (2011). The structure of the upper mantle beneath the Delamerian and Lachlan orogens from simultaneous inversion of multiple teleseismic datasets, *Gondwana Research* **19**: 788–799.

Rawlinson, N., Salmon, M. & Kennett, B. L. N. (2014). Transportable seismic array tomography in southeast Australia: Illuminating the transition from Proterozoic to Phanerozoic lithosphere, *Lithos* **189**: 65–76.

Reid, A. J., Messeiller, M. & Fricke, C. E. (2011). *PACE Geochronology: Results of Collaborative Geochronology Projects 200910*, Department of Primary Industries and Resources, chapter Project PGC01-01: UPb geochronology of samples from the Paralana 2 deep geothermal well, Arrowie Basin, pp. 10–26.

Reiter, M. (2008). Geothermal anomalies in the crust and upper mantle along Southern Rocky Mountain transitions, *Geological Society of America, Bulletin* **120**: 431–441.

Reiter, M. & Clarkson, G. (1983). Geothermal studies in the San Juan Basin and the Four Corners area of the Colorado Plateau. II. Steady-state models of the thermal source of the San Juan volcanic field, *Tectonophysics* **91**: 253–269.

Roach, I. C., Jaireth, S. & Costelloe, M. T. (2014). Applying regional airborne electromagnetic (AEM) surveying to understand the architecture of sandstone-hosted uranium mineral systems in the Callabonna Sub-basin, Lake Frome region, South Australia, *Australian Journal of Earth Sciences* **61**: 659–688.

Rolandone, F., Jaupart, C., Mareschal, J. C., Gariépy, C., Bienfait, G., Carbonne, C. & Lapointe, R. (2002). Surface heat flow, crustal temperatures and mantle heat flow in the Proterozoic Trans-Hudson Orogen, Canadian Shield, *Journal of Geophysical Research* **107**: ETG 7–1 – 7–19.

Sandiford, M. (2003). Neotectonics of southeastern Australia: linking the Quaternary faulting record with seismicity and in situ stress, *Geological Society of Australia Special Publication* **22**: 107–119.

Sass, J. H., Jaeger, J. C. & Munroe, R. J. (1976). Heat flow and near surface radioactivity in the Australian continental crust, *US Geological Survey, Open-File Report* pp. 76–250.

Sass, J. H., Williams, C. F., Lachenbruch, A. H., Galanis Jr., S. P. & Grubb, F. V. (1997). Thermal regime of the San Andreas fault near Parkfield, California, *Journal of Geophysical Research* **102**: 27,575–27,585.

Slagstad, T., Midttomme, K., Ramstad, R. K. & Slagstad, D. (2008). *Geology for society*, Vol. 11, Geological Survey of Norway Special Publication, chapter Factors influencing shallow (¡1000m depth) temperatures and their significance for extraction of ground-source heat, pp. 99–109.

Somerton, W. H. (1992). *Thermal properties and temperature-related behavior of rock/fluid systems*, Elsevier, New York.

Tester, J. (2006). The Future of Geothermal Energy Impact of Enhanced Geothermal Systems (EGS) on the United States in the 21st Century, *Technical report*, Idaho National Laboratory, Idaho Falls. ISBN: 0-615-13438-6.

Titus, S. J., DeMets, C. & Tikoff, B. (2006). Thirty-five-year creep rates for the creeping segment of the San Andreas Fault and the effects of the 2004 Parkfield Earthquake: Constraints from alignment arrays, continuous Global Positioning System, and creepmeters, *Bulletin of the Seismological Society of America* **96**: S250–S268.

Wade, C. E., Reid, A. J., Wingate, M. T. D., Jagodzinski, E. A. & Barovich, K. (2012). Geochemistry and geochronology of the c. 1585 Ma Benagerie Volcanic Suite, southern Australia: Relationship to the Gawler Range Volcanics and implications for the petrogenesis of a Mesoproterozoic silicic large igneous province, *Precambrian Research* **206-207**: 17–35.

Walsh, J. B. & Decker, E. R. (1966). Effect of pressure and saturating fluid on the thermal conductivity of compact rock, *Journal of Geophysical Research* **71**: 3,053–3,061.

Wessel, P., Smith, W. H. F., Scharroo, R., Luis, J. F. & Wobbe, F. (2013). Generic Mapping Tools: Improved version released, *EOS, Transactions American Geophysical Union* **94**: 409–410.

Wingate, M. T. D., Campbell, I. H., Compston, W. & Gibson, G. M. (1998). Ion microprobe U-Pb ages for Neoproterozoic basaltic magmatism in south-central Australia and implications for the breakup of Rodinia, *Precambrian Research* **87**: 135–159.

Wyborn, L. A. I., Budd, A. R. & Bastrakova, I. V. (1998). The Metallogenic Potential of Australian Proterozoic Granites. Grante GIS (Partial Release) CD ROM. Australian Geological Survey Organisation, Canberra.

Zielhaus, A. & van der Hilst, R. D. (1996). Upper-mantle shear velocity beneath eastern Australian from inversion of waveforms from SKIPPY portable arrays, *Geophysical Journal International* **127**: 1–16.

APPENDIX A: SAMPLING AND QUALITY CONTROL

Drill core samples were selected visually with the intent to acquire the best representation possible for each stratigraphy, often at a rate of approximately one sample for ten metres of core. Samples were taken from either side of a major stratigraphic boundary where possible, and samples that represented a significant but short change in stratigraphy were avoided.

Some interbedded units broke easily, and often were not sampled as they were unsuitable for the experimental procedures planned. This leads to an inherent bias as these units are not contributing to the measured thermal conductivity mean of a package, although they still comprise a significant part of the package and contribute to the effect on heat flow.

Multiple workers were involved in the sampling process. Despite care taken to ensure that the same sampling protocol was used, some selection bias may have occurred.

A surface roughness on core samples of greater than 1 mm may result in systematic errors of thermal conductivity measurements (Popov et al 1999). It was decided that the Frome samples were sufficiently smooth to not require polishing.

Temperature measurements on the edges of standards and samples tend to spike due to edge effects, making them unreliable. These zones are removed from the thermal conductivity calculations by observation, utilising the TCS program to reduce the width of the calculation zone for each standard and sample.

Some samples have small fractures which tend to cause spikes in temperature measurements, impacting the mean thermal conductivity determination of the sample. This occurs in both the saturated and unsaturated measurements, and is due to the increased volume of water and air within the samples which have greatly lower thermal conductivities compared to that of typical rock samples.

Quartz content has a significant effect on the thermal conductivity of samples, as pure quartz has a thermal conductivity significantly smaller than typical rock samples ($\sim$1.5 W m^{-1} K^{-1}). As a result, the thermal conductivity measurement for a sample can often be dominated by the quartz content.

When scanning saturated samples, small droplets of water can collect on the underside of the cylindrical core despite care taken to dry the exterior of the core. This may cause minor spikes in the thermal conductivity measurements due to the conductivity of water being an order of magnitude lower than typical rocks.

Due to multiple workers being involved in the core scanning process, an inherent bias exists in the selection of sample and standard edges on the TCS program for thermal conductivity estimates, despite care taken to conform to the same standards. This includes the removal of edge effects, and may result in minor differences in thermal conductivity measurements.

It is interesting to note that a sample with sufficiently fine grains will, while inherently inhomogeneous, appear homogeneous on the thermal conductivity profile due to the measurement resolution of the TCS.

The paint on core samples occasionally peels off in some parts of the core after saturation. A volume of air may occupy the space between the paint and the sample. Thus

when the TCS scans that paint section, the thermal conductivity will be significantly lower than expected due to the pocket of air.

APPENDIX B: EXTENDED THERMAL CONDUCTIVITY, THERMAL GRADIENT AND HEAT FLOW METHODS

Heat flow is determined individually for each stratigraphic package within a drill hole. The mean thermal conductivity for each stratigraphic package was determined using a harmonic mean. Each thermal conductivity measurement was given a weighting based on its distance from the next measurement above and below in the drill hole. Each measurement is assumed to be representative of the stratigraphy for half the distance to the measurement above, and half the distance to the measurement below. The shallowest and deepest measurements for each stratigraphy were assumed to be representative of the stratigraphy to the top and to the bottom of the package respectively. Greater distances between sample points increases their individual weighting, as they are assumed to be representative of more stratigraphy.

A thermal gradient vs depth profile was determined using a windowing method. The size of window used for each drill hole was determined by observation, selecting the window size where the profile became sufficiently smooth.

For the purposes of a heat flow estimate, the mean thermal gradient for each stratigraphic package is determined by taking the temperatures at the top and bottom of the stratigraphic package and using the following equation:

$$\Gamma = \frac{(T_b - T_t)}{(\Delta z)}, \tag{11}$$

where T_t and T_b are the top and bottom temperatures and Δz is the change in depth.

The product equation is then used to determine heat flow from the thermal conductivity and thermal gradient of each stratigraphic package.

Some stratigraphic packages progress into shallow depths where surface temperature effects take place, and so any stratigraphy shallower than 100 m is cut off and assumed to end at 100 m for the purposes of its average heat flow determination.

Frome 13 suffered from a poor sample spacing in both temperature and thermal conductivity, and so heat flow is determined in intervals between temperature measurements where a major change in stratigraphy does not occur. The thermal conductivity for these intervals are then determined using the harmonic mean of samples within the interval.

APPENDIX C: RAW DATA

Table 3: Density and porosity of Frome drill holes.

Drill hole	Sample depth (m)	Density (%)	Porosity
Frome 8	215.75	2.76906	1.59594
Frome 8	237	2.74957	0.75265
Frome 8	248.1	2.75177	0
Frome 8	253.05	2.73699	1.35616
Frome 8	258.55	2.74133	0
Frome 8	270.6	2.74774	0
Frome 8	284.05	2.75039	0.22613
Frome 8	290.9	2.73899	0.10808
Frome 8	305.45	2.75867	0
Frome 8	320.8	2.74873	0.16896
Frome 8	327.65	2.75114	0
Frome 8	333.65	2.75468	0.29557
Frome 8	336.55	2.76288	0.07289
Frome 8	349.4	2.75034	0
Frome 8	364.8	2.75807	0.3229
Frome 8	371.15	2.74647	0
Frome 8	381.7	2.75340	0
Frome 8	393.65	2.78559	0.03752
Frome 8	398.55	2.76619	0.13905
Frome 8	405.3	2.76489	0.033
Frome 8	410.65	2.76631	0.14885
Frome 8	423.35	2.75936	0.02216
Frome 8	435.65	2.76947	0.07729
Frome 8	447.65	2.75972	0
Frome 8	450.85	2.75710	0.40541
Frome 8	456.75	2.66521	0.22801
Frome 8	463.4	2.75173	0.48963
Frome 8	476.45	2.75877	0
Frome 8	486.4	2.75891	0
Frome 8	493.15	2.73149	0

Table 3 – *Continued from previous page*

Drill hole	Depth	Density	Porosity
Frome 9	130.25	2.70945	0.93089
Frome 9	135.65	2.71993	1.58844
Frome 9	143.5	2.61907	0.80671
Frome 9	153.55	2.76321	0
Frome 9	159.95	2.77083	0.88213
Frome 9	168.75	2.73298	0.9993
Frome 9	180.65	2.76570	0.01292
Frome 9	189.5	2.78161	0.72006
Frome 9	197.6	2.76789	0.71418
Frome 9	210.95	2.77481	0.40749
Frome 9	219	2.76376	0.17339
Frome 9	219.2	2.75780	0.98342
Frome 9	227.55	2.74386	0.20455
Frome 9	236.55	2.76054	0.04737
Frome 9	245.35	2.73666	0.43927
Frome 9	255.65	2.72761	0.46356
Frome 9	264.55	2.76812	0
Frome 9	274.2	2.71707	0.33376
Frome 9	280.75	2.73481	1.00395
Frome 9	289.75	2.72874	0.19086
Frome 9	298.25	2.71758	0.12634
Frome 9	305.75	2.75720	1.33941
Frome 9	312.8	2.6456	0.48382
Frome 9	314.45	2.71253	1.0705
Frome 9	318.5	2.64454	0
Frome 9	324	2.76159	1.00172
Frome 9	329.55	2.64178	0.92443
Frome 9	333.45	2.60734	0
Frome 9	339.8	2.76519	0.25018
Frome 9	348.8	2.76243	0.08671
Frome 9	355.15	2.72118	0.60311
Frome 9	362.55	2.73772	1.49589
Frome 9	372.6	2.75551	0.02397
Frome 9	384.3	2.78492	1.93302

Continued on next page

Table 3 – *Continued from previous page*

Drill hole	Depth	Density	Porosity
Frome 9	391.75	2.76344	0.04317
Frome 9	398.85	2.78058	0.18617
Frome 9	404.15	2.70136	0.33438
Frome 9	415.5	2.80875	0.51187
Frome 9	426.25	2.80836	0.27745
Frome 9	436.9	2.68568	3.29146
Frome 9	445.35	2.69488	1.1361
Frome 9	455.35	2.70546	1.80332
Frome 9	458.5	2.82180	4.11444
Frome 9	466.45	2.77136	0.67998
Frome 9	480	2.81914	0.96986
Frome 9	494.35	2.81499	1.47192
Frome 9	504.75	2.83897	2.71179
Frome 12	278	No data	No data
Frome 12	279	No data	No data
Frome 12	330	No data	No data
Frome 12	421	No data	No data
Frome 12	474	No data	No data
Frome 12	529	No data	No data
Frome 12	582	No data	No data
Frome 12	635	No data	No data
Frome 12	688	No data	No data
Frome 12	740	No data	No data
Frome 12	796	No data	No data
Frome 12	827	No data	No data
Frome 12	905	No data	No data
Frome 12	936	No data	No data
Frome 12	950	No data	No data
Frome 12	959	No data	No data
Frome 12	974	No data	No data
Frome 12	1018	No data	No data
Frome 12	1030	No data	No data
Frome 12	1030	No data	No data
Frome 12	1057	No data	No data

Continued on next page

Table 3 – *Continued from previous page*

Drill hole	Depth	Density	Porosity
Frome 12	1136	No data	No data
Frome 12	1157	No data	No data
Frome 12	1168	No data	No data
Frome 12	1188	No data	No data
Frome 12	1236	No data	No data
Frome 12	1236	No data	No data
Frome 12	1271	No data	No data
Frome 12	1337	No data	No data
Frome 12	1415	No data	No data
Frome 12	1425	No data	No data
Frome 12	1437	No data	No data
Frome 12	1469	No data	No data
Frome 12	1472	No data	No data
Frome 12	1492	2.63716	0.26348
Frome 12	1654	2.62599	1.08258
Frome 12	1756	2.63953	0.81078
Frome 13	273	No data	No data
Frome 13	294	No data	No data
Frome 13	398	2.63331	0.86988
Frome 13	452	No data	No data
Frome 13	530	No data	No data
Frome 13	530	No data	No data
Frome 13	617	No data	No data
Frome 13	688	No data	No data
Frome 13	858	No data	No data
Frome 13	858	No data	No data
Frome 13	930	No data	No data
Frome 13	963	No data	No data
Frome 13	968	No data	No data
Frome 13	1025	No data	No data
Frome 13	1289	2.72942	1.23085
Frome 13	1320	No data	No data
Frome 13	1320	No data	No data
Frome 13	1410	No data	No data

Continued on next page

Table 3 – *Continued from previous page*

Drill hole	Depth	Density	Porosity
Frome 13	1422	No data	No data
Frome 13	1448	No data	No data
Frome 13	1501	No data	No data
Frome 13	1501	No data	No data
Frome 13	1558	No data	No data
Frome 13	1598	2.70093	0.53133
Frome 13	1623	No data	No data
Frome 13	1678	No data	No data
Frome 13	1678	No data	No data
Frome 13	1726	No data	No data
Frome 13	1759	No data	No data
Frome 13	1791	2.65165	1.16408

Table 4: Raw thermal conductivity data for Frome samples. Conductivities are in $\mathrm{Wm^{-1}\,K^{-1}}$. d and s subscripts represent dry and saturated measurements respectively.

Drill hole	Depth (m)	Mean$_d$	Min$_d$	Max$_d$	Inhomo$_d$	Mean$_s$	Min$_s$	Max$_s$	Inhomo$_s$
Frome 8	493.15	3.033	2.81	3.304	No data	3.023	2.46	3.296	No data
Frome 8	486.4	3.268	3.073	3.504	No data	3.003	2.819	3.18	No data
Frome 8	476.45	3.335	2.992	3.697	No data	3.264	2.993	3.481	No data
Frome 8	463.4	2.166	1.966	2.393	No data	3.327	3.13	3.639	No data
Frome 8	456.75	3.175	2.989	3.424	No data	3.324	3.19	3.494	No data
Frome 8	450.85	3.071	2.889	3.327	No data	3.184	3.022	3.504	No data
Frome 8	447.65	3.192	2.977	3.549	No data	3.153	3.015	3.404	No data
Frome 8	435.65	3.198	2.932	3.63	No data	3.118	2.864	3.549	No data
Frome 8	423.35	3.102	2.93	3.417	No data	3	2.733	3.233	No data
Frome 8	410.65	3.191	3.038	3.388	No data	2.994	2.699	3.111	No data
Frome 8	405.3	3.348	3.126	3.66	No data	2.905	2.729	3.229	No data
Frome 8	398.55	3.341	3.089	3.604	No data	2.935	2.771	3.114	No data
Frome 8	393.65	3.12	2.942	3.327	No data	3.173	3.004	3.29	No data
Frome 8	381.7	3.258	2.991	3.476	No data	2.793	2.659	3.071	No data
Frome 8	371.15	3.239	3.001	3.431	No data	2.899	1.584	3.234	No data
Frome 8	364.8	3.296	3.028	3.697	No data	2.985	2.842	3.294	No data
Frome 8	349.4	3.207	2.941	2.538	No data	2.852	2.675	3.23	No data
Frome 8	336.55	3.447	3.208	3.714	No data	3.212	3.021	3.7	No data
Frome 8	333.65	3.198	3.027	3.364	No data	3.149	2.653	3.335	No data
Frome 8	327.65	3.191	3.017	3.377	No data	3.006	2.855	3.213	No data
Frome 8	320.8	3.296	3.045	3.522	No data	3.112	2.994	3.303	No data

Continued on next page

Table 4 – *Continued from previous page*

Drill hole	Depth (m)	$Mean_d$	Min_d	Max_d	$Inhomo_d$	$Mean_s$	Min_s	Max_s	$Inhomo_s$
Frome 8	305.45	3.081	2.929	3.297	No data	3.157	2.906	3.311	No data
Frome 8	290.9	3.317	3.138	3.5	No data	2.737	2.597	2.877	No data
Frome 8	284.05	3.244	3.019	3.438	No data	3.172	3.013	3.308	No data
Frome 8	270.6	3.162	2.851	3.369	No data	2.744	2.471	2.879	No data
Frome 8	258.55	3.12	2.968	3.286	No data	3.198	3.042	3.372	No data
Frome 8	253.05	3.108	2.987	3.277	No data	3.266	3.065	3.537	No data
Frome 8	248.1	3.052	0.6	3.58	No data	3.169	3.001	3.476	No data
Frome 8	237	2.768	2.522	2.972	No data	3.253	3.091	3.454	No data
Frome 8	215.75	3.409	3.232	3.756	No data	3.298	3.161	3.401	No data
Frome 9	130.25	2.57	2.285	2.948	No data	3.073	2.772	3.476	No data
Frome 9	135.65	2.911	2.345	3.181	No data	2.624	2.455	2.846	No data
Frome 9	143.5	3.188	2.716	3.466	No data	3.031	2.695	3.207	No data
Frome 9	153.55	3.106	2.915	3.318	No data	2.969	2.861	3.117	No data
Frome 9	159.95	2.371	2.26	2.549	No data	3.057	2.912	3.179	No data
Frome 9	168.75	2.946	2.682	3.136	No data	3.049	2.921	3.222	No data
Frome 9	180.65	2.95	2.758	3.147	No data	3.036	2.854	3.262	No data
Frome 9	189.5	3.46	3.24	3.634	No data	3.118	2.877	3.262	No data
Frome 9	197.6	3.274	3.038	3.466	No data	3.172	2.964	3.355	No data
Frome 9	210.95	3.299	3.063	3.552	No data	2.899	2.738	3.161	No data
Frome 9	219	3.362	3.097	3.743	No data	3.215	3.058	3.513	No data
Frome 9	219.2	2.978	2.833	3.108	No data	3.208	3.069	3.33	No data
Frome 9	227.55	3.351	3.14	3.592	No data	2.846	2.671	3.026	No data
Frome 9	236.55	3.194	2.964	3.475	No data	2.952	2.792	3.201	No data

Continued on next page

Table 4 – *Continued from previous page*

Drill hole	Depth (m)	$Mean_d$	Min_d	Max_d	$Inhomo_d$	$Mean_s$	Min_s	Max_s	$Inhomo_s$
Frome 9	245.35	2.339	2.132	2.509	No data	3.027	2.894	3.11	No data
Frome 9	255.65	2.873	2.595	3.197	No data	3.345	2.904	3.569	No data
Frome 9	264.55	2.991	2.788	3.254	No data	2.985	2.798	3.165	No data
Frome 9	274.2	3.36	3.24	3.483	No data	2.774	2.385	3.087	No data
Frome 9	280.75	3.189	3.023	3.421	No data	1.707	1.431	1.949	No data
Frome 9	289.75	2.578	2.21	2.816	No data	2.749	2.23	3.134	No data
Frome 9	298.25	3.412	3.255	3.601	No data	2.316	2.065	2.465	No data
Frome 9	305.75	2.463	2.343	2.686	No data	3.459	3.25	3.615	No data
Frome 9	312.8	2.535	2.368	2.698	No data	2.7	2.553	2.909	No data
Frome 9	314.45	2.508	2.431	2.607	No data	2.766	2.652	2.939	No data
Frome 9	318.5	2.173	1.998	2.307	No data	2.783	2.653	2.914	No data
Frome 9	324	2.537	2.376	2.688	No data	3.395	3.275	3.54	No data
Frome 9	329.55	2.939	2.756	3.204	No data	No data	No data	No data	No data
Frome 9	333.45	2.577	2.439	2.864	No data	2.575	2.405	2.736	No data
Frome 9	339.8	3.439	3.155	3.666	No data	2.286	1.751	2.908	No data
Frome 9	348.8	3.504	3.26	3.779	No data	2.715	2.496	3.007	No data
Frome 9	355.15	2.502	2.385	2.652	No data	3.412	3.164	3.757	No data
Frome 9	362.55	2.895	2.679	3.25	No data	2.758	2.594	2.938	No data
Frome 9	372.6	3.529	3.295	3.733	No data	2.948	2.772	3.076	No data
Frome 9	384.3	3.41	3.202	3.628	No data	3.005	2.824	3.117	No data
Frome 9	391.75	3.366	3.12	3.588	No data	2.813	2.573	3.048	No data
Frome 9	398.85	3.324	3.134	3.512	No data	2.416	2.312	2.544	No data
Frome 9	404.15	2.852	2.658	3.109	No data	2.628	2.417	2.85	No data

Continued on next page

Table 4 – *Continued from previous page*

Drill hole	Depth (m)	Mean$_d$	Min$_d$	Max$_d$	Inhomo$_d$	Mean$_s$	Min$_s$	Max$_s$	Inhomo$_s$
Frome 9	415.5	4.061	3.673	4.528	No data	3.595	3.383	3.84	No data
Frome 9	426.25	4.023	3.606	5.15	No data	2.193	2.025	2.35	No data
Frome 9	436.9	2.87	2.539	3.146	No data	3.187	2.926	3.485	No data
Frome 9	445.35	2.303	2.088	2.511	No data	2.008	2.857	3.222	No data
Frome 9	455.35	2.867	2.686	3.04	No data	3.053	2.799	3.292	No data
Frome 9	458.5	3.534	3.338	3.688	No data	3.843	3.581	4.074	No data
Frome 9	466.45	3.285	3.082	3.527	No data	3.022	2.827	3.248	No data
Frome 9	480	4.048	3.817	4.316	No data	3.258	3.084	3.493	No data
Frome 9	480	3.964	3.461	4.42	No data	3.055	2.851	3.326	No data
Frome 9	494.35	3.662	3.437	3.883	No data	3.931	3.619	4.265	No data
Frome 9	504.75	3.226	2.748	3.592	No data	3.508	2.773	4.006	No data
Frome 12	278	2.879	2.637	3.085	0.156	3.285156	3.056844	3.610712	No data
Frome 12	279	2.806	2.19	3.263	0.383	2.97017	2.479722	3.56209	No data
Frome 12	330	3.121	2.982	3.255	0.088	3.146689	2.992367	3.428908	No data
Frome 12	421	2.902	2.792	3.015	0.077	3.182627	3.000823	3.411996	No data
Frome 12	474	2.968	2.867	3.095	0.078	3.066357	2.879268	3.272472	No data
Frome 12	529	3.118	3.024	3.219	0.063	3.121321	2.984968	3.241819	No data
Frome 12	582	2.92	2.393	3.191	0.274	3.352804	2.700635	3.684702	No data
Frome 12	635	3.115	2.933	3.314	0.122	3.451105	3.239705	3.76292	No data
Frome 12	688	3.154	3.066	3.283	0.069	3.556805	3.408825	3.698443	No data
Frome 12	740	3.183	3.04	3.433	0.123	3.314752	3.099124	3.610712	No data
Frome 12	796	3.134	3.042	3.234	0.061	3.495499	3.277757	3.640308	No data
Frome 12	827	3.191	3.055	3.334	0.087	3.239705	3.003994	3.395084	No data

Table 4 – *Continued from previous page*

Drill hole	Depth (m)	$Mean_d$	Min_d	Max_d	$Inhomo_d$	$Mean_s$	Min_s	Max_s	$Inhomo_s$
Frome 12	905	3.143	3.044	3.222	0.056	3.307353	3.109694	3.45639	No data
Frome 12	936	No data	No data	No data	No data	3.385571	3.26613	3.561033	No data
Frome 12	950	3.472	2.937	3.193	0.0835	3.109694	2.717547	3.355975	No data
Frome 12	959	3.208	2.929	3.582	0.204	4.362183	4.036599	4.651353	No data
Frome 12	974	4.1	3.794	4.355	0.137	4.612797	4.292568	4.919103	No data
Frome 12	1018	3.485	3.119	3.776	0.189	3.573717	3.331664	3.841138	No data
Frome 12	1030	3.288	3.192	3.484	0.089	3.383457	3.172057	3.693158	No data
Frome 12	1030	3.414	3.339	3.515	0.052	3.335892	2.694293	3.201653	No data
Frome 12	1057	3.382	3.166	3.572	0.12	3.535665	3.388742	3.693158	No data
Frome 12	1136	3.487	3.294	3.694	0.115	No data	No data	No data	No data
Frome 12	1157	3.479	3.286	3.726	0.126	No data	No data	No data	No data
Frome 12	1168	3.534	3.292	3.764	0.134	No data	No data	No data	No data
Frome 12	1188	2.235	2.029	2.378	0.156	2.805278	2.700635	2.928947	No data
Frome 12	1236	3.195	3.132	3.243	0.035	2.991146	2.838751	3.119368	No data
Frome 12	1236	3.135	3.038	3.246	0.066	3.339027	3.221315	3.428362	No data
Frome 12	1271	2.546	2.379	2.832	0.178	2.99535	2.788303	3.389475	No data
Frome 12	1337	3.65	3.429	3.892	0.127	3.763631	3.427311	4.102053	No data
Frome 12	1415	3.594	3.331	3.926	0.166	3.818283	3.469351	4.249193	No data
Frome 12	1425	3.601	2.759	4.15	0.386	3.088889	2.428861	4.071574	No data
Frome 12	1437	3.469	3.328	3.647	0.092	3.229723	2.950157	3.527156	No data
Frome 12	1469	3.114	2.913	3.331	0.134	3.124623	2.820884	3.609134	No data
Frome 12	1472	2.996	2.74	3.273	0.178	3.41575	2.917576	3.527156	No data
Frome 12	1492	3.036	2.84	3.292	0.149	3.094144	3.424158	2.866077	No data

Continued on next page

57

Table 4 – *Continued from previous page*

Drill hole	Depth (m)	Mean$_d$	Min$_d$	Max$_d$	Inhomo$_d$	Mean$_s$	Min$_s$	Max$_s$	Inhomo$_s$
Frome 12	1654	2.951	2.563	3.234	0.227	3.137235	2.735753	3.703724	No data
Frome 12	1756	3.04	2.77	3.309	0.177	3.309599	2.957514	3.700571	No data
Frome 13	273	2.733	2.62	2.83	0.077	2.899351	2.776739	3.106523	No data
Frome 13	294	2.672	2.557	2.834	0.104	2.645671	2.44167	2.780967	No data
Frome 13	398	3.006	2.879	3.124	0.082	3.386628	3.176285	3.685759	No data
Frome 13	452	No data	No data	No data	No data	2.893009	2.637215	3.091725	No data
Frome 13	530	2.991	2.696	3.153	0.153	3.121321	2.978626	3.370773	No data
Frome 13	530	2.858	2.64	3.077	0.153	2.964885	2.697464	3.376058	No data
Frome 13	617	2.796	2.439	2.969	0.19	2.981797	2.736573	3.278814	No data
Frome 13	688	3.014	2.906	3.097	0.0625	3.256617	3.052616	3.415167	No data
Frome 13	858	2.628	2.59	2.696	0.041	2.636959	2.559185	2.709478	No data
Frome 13	858	2.485	2.454	2.513	0.021	2.898658	2.666387	3.566043	No data
Frome 13	930	2.346	2.267	2.453	0.079	2.509788	2.28067	2.830343	No data
Frome 13	963	3.271	3.051	4.071	0.312	3.551329	3.248641	4.667491	No data
Frome 13	968	3.395	3.194	3.617	0.124	4.074727	3.747866	4.3091	No data
Frome 13	1025	No data	No data	No data	No data	2.933341	2.830343	3.039492	No data
Frome 13	1289	3.071	2.911	3.274	0.118	3.094144	2.997452	3.201346	No data
Frome 13	1320	3.097	2.994	3.186	0.062	3.390526	3.246539	3.494575	No data
Frome 13	1320	3.003	2.848	3.163	0.105	3.334823	2.980636	4.907119	No data
Frome 13	1410	2.987	2.879	3.096	0.073	3.280171	3.190836	3.364251	No data
Frome 13	1422	2.909	2.726	3.115	0.134	2.95331	2.678999	3.183479	No data
Frome 13	1448	4.177	3.973	4.439	0.112	4.243008	4.001184	4.569312	No data
Frome 13	1501	3.064	2.994	3.155	0.053	3.255998	3.14249	3.440974	No data

Continued on next page

Table 4 – *Continued from previous page*

Drill hole	Depth (m)	Mean$_d$	Min$_d$	Max$_d$	Inhomo$_d$	Mean$_s$	Min$_s$	Max$_s$	Inhomo$_s$
Frome 13	1501	2.971	2.971	3.206	0.152	3.336925	3.16351	3.627001	No data
Frome 13	1558	3.108	3.036	3.213	0.171	3.165612	3.021625	3.358996	No data
Frome 13	1598	2.528	2.286	2.877	0.234	2.937545	2.747314	3.209754	No data
Frome 13	1623	2.562	2.484	2.719	0.092	3.088889	2.939647	3.932842	No data
Frome 13	1678	3.02	2.864	3.101	0.078	3.491422	3.220264	3.89921	No data
Frome 13	1678	2.918	2.838	2.984	0.05	3.305395	3.177173	3.413648	No data
Frome 13	1726	2.921	2.678	3.115	0.15	3.348486	3.116215	3.551329	No data
Frome 13	1759	No data	No data	No data	No data	3.635409	3.324313	4.838804	No data
Frome 13	1791	3.127	2.916	3.288	0.119	No data	No data	No data	No data

Table 5: Raw thermal conductivity data for Paralana samples. Conductivities are in $\text{Wm}^{-1} \text{K}^{-1}$. A, B, and C refer to sub-samples taken. *Italicised results were from damaged samples and were not used to calculate the mean.*

Sample No.	Depth (m)	A	B	C	Mean
PTR-001	1752.08	2.618	2.631	2.654	2.63 ± 0.02
PTR-002	1681.04	2.707	2.755	2.632	2.70 ± 0.06
PTR-003	1620.21	2.653	2.55	2.681	2.61 ± 0.05
PTR-004	1525.50	4.532	4.645	4.671	4.62 ± 0.07
PTR-005	1480.60	3.844	3.606	2.552	3.23 ± 0.69
PTR-006	1454.05	2.365	2.692	2.946	2.65 ± 0.29
PTR-007	1419.08	2.903	3.449	*2.529*	3.15 ± 0.39
PTR-008	1357.16	2.159	2.354	2.735	2.39 ± 0.29
PTR-009	1327.50	3.526	3.265	3.565	3.45 ± 0.16
PTR-010	1285.42	3.905	3.582	3.777	3.75 ± 0.16
PTR-011	1259.51	4.124	4.493	4.443	4.35 ± 0.20
PTR-012	1242.75	2.649	3.432	3.05	3.01 ± 0.39
PTR-013	1196.52	2.137	2.365	2.474	2.32 ± 0.17
PTR-014	1171.37	2.451	2.475	2.481	2.47 ± 0.02
PTR-015	1151.12	2.358	2.587	2.481	2.47 ± 0.11
PTR-016	1105.43	2.082	2.031	1.976	2.03 ± 0.05
PTR-017	1081.06	1.797	1.765	1.831	4.63 ± 0.34
PTR-018	1039.84	4.391	4.511	5.025	4.63 ± 0.34
PTR-019	1006.43	5.618	5.509	5.556	5.56 ± 0.05
PTR-020	993.03	4.701	3.708	4.593	4.28 ± 0.55
PTR-021	907.39	3.5	3.474	3.549	3.51 ± 0.04
PTR-022	835.59	3.876	3.785	3.835	3.83 ± 0.05
PTR-023	775.57	2.861	2.799	*2.211*	2.83 ± 0.04
PTR-024	697.95	6.99	7.156	6.945	7.03 ± 0.11
PTR-025	654.42	5.64	6.165	6.002	5.93 ± 0.27
PTR-026	627.69	6.757	6.302	5.871	6.29 ± 0.44
PTR-027	594.78	5.857	6.153	5.553	6.00 ± 0.21
PTR-028	550.52	5.926	5.865	5.886	5.89 ± 0.03
PTR-029	518.28	2.158	1.798	1.603	1.83 ± 0.28
PTR-030	No data	2.07	1.501	1.521	1.66 ± 0.32

Table 5 – *Continued from previous page*

Sample No.	Depth (m)	A	B	C	Mean
PTR-031	No data	1.902	1.786	1.825	1.84 ± 0.06
PTR-032	No data	2.433	2.097	2.627	2.36 ± 0.27
PTR-033	No data	1.732	1.689	1.736	1.72 ± 0.03
PTR-034	No data	2.936	3.08	2.818	2.94 ± 0.13
PTR-035	No data	2.939	2.418	2.664	2.66 ± 0.26
PTR-036	No data	3.287	*2.865*	3.094	3.19 ± 0.14

APPENDIX D: ERROR PROPAGATION

All uncertainties are propagated using the general formula of Bevington (1969) in Equation 1.

Thermal gradient

The error in thermal gradient between two points is determined from Equation 11, giving:

$$\sigma_\Gamma = \left(\frac{1}{\Delta z}\right)\left((T_b\sigma_b)^2 + (T_t\sigma_t)^2\right)^{\frac{1}{2}}, \tag{12}$$

where Δz is the change in depth, T_t and T_b are the temperatures at the top and bottom points and σ_t and σ_b are the uncertainties in the top and bottom temperatures.

Thermal conductivity

Thermal resistance, R, is defined again here as:

$$R = \sum_{i=1}^{N} \frac{h_i}{\lambda_i}, \tag{13}$$

where h_i is the thickness of an interval.

The error in harmonic mean of thermal conductivity for a stratigraphic package is determined from Equation 7, giving:

$$\sigma_{\lambda_{av}} = \left(\sum_{j=1}^{N} \sigma_{\lambda_j}^2 \left(\frac{h_t h_j}{R^2 \lambda_j^2}\right)^2\right)^{\frac{1}{2}}, \tag{14}$$

where h_t is the total depth of stratigraphy, h_i and λ_i are the thickness and conductivity of the ith layer, h_j, λ_j and σ_{λ_j} are the thickness, thermal conductivity and standard deviation of the jth layer.

Product method heat flow

The error in heat flow estimated using the product method is determined by Equation 8, giving:

$$\sigma_q = \left(\sigma_\lambda^2 \Gamma^2 + \sigma_\Gamma^2 \lambda^2\right)^{\frac{1}{2}}. \tag{15}$$

Uncertainty in surface heat flow for a drill hole is given by:

$$\sigma_{q_s} = \frac{1}{N}\left(\sum_{i=1}^{N} \sigma_{q_i}^2\right)^{\frac{1}{2}}, \tag{16}$$

where q_i is the heat flow of an interval and N is the number of intervals.

Thermal resistance

The error in the thermal resistance of an interval is derived using the equation for thermal resistance (Equation 9), giving:

$$\sigma_{R_i} = \left(\sigma_\lambda^2 \left(-\Delta z \lambda \right)^2 \right)^{\frac{1}{2}}, \tag{17}$$

where Δz is the thickness of the interval and λ is the harmonic mean of thermal conductivity of the interval.

The cumulative thermal resistance at a given depth is determined by including the thermal resistance of all shallower intervals, so the error in cumulative thermal resistance is:

$$\sigma_{R_t} = \left(\sum_{i=1}^{N} \sigma_{R_i} \right)^{\frac{1}{2}}, \tag{18}$$

APPENDIX E: RECOMMENDATIONS FOR FUTURE STUDIES

If thermal diffusivity is calculated at the same time as thermal conductivity, another thermal parameter, specific heat, can be determined using the following equation:

$$C_p^{-1} = \frac{\kappa \rho}{\lambda}, \tag{19}$$

where ρ is the density of the measured material and κ is the thermal diffusivity. As a systematic bias occurs in the measurement for thermal conductivity when measured simultaneously with thermal diffusivity, the correction factor derived by Bowker (2013) must be applied.

It is recommended that three or more measurements of thermal conductivity samples are made to reduce the uncertainty. As outlined in Bowker (2013), rapid repeat measurements of a sample reduce precision, thus sufficient time should be allowed between each measurement.

It is recommended that the temperature at the top and bottom of the room are measured at the start of each measurement session to ensure that there is no substantial difference. If there is, care must be taken with regards to where samples and standards are kept just prior to measuring thermal conductivity. Also, large variations in temperature between days may need to be factored into measurements. As a result, it is recommended that samples are measured in a room without natural lighting, preferably below ground level, and that the door to the lab is kept closed.

Extreme caution should be taken with samples as they break easily along bedding planes, especially when saturated. If a sample breaks it is difficult to get a representative dry and saturated thermal conductivity, density and porosity measurements for the same sample.